Precambrian faulting episodes and insights into the tectonothermal history of North Australia: Microstructural evidence and K–Ar, ^{40}Ar–^{39}Ar, and Rb–Sr dating of syntectonic illite from the intracratonic Millungera Basin.

Ibrahim Tonguç Uysal[1], Claudio Delle Piane[2], Andrew James Todd[2] and Horst Zwingmann[3]*

[1]Ankara University, Geological Engineering Department, Gölbaşı, Ankara, Turkey

[2]CSIRO Energy, 26 Dick Perry Avenue, Kensington WA 6151, Australia

[3]Department of Geology and Mineralogy, Kyoto University, Kitashirakawa Oiwake-cho, Kyoto 606-8502, Japan.

* Corresponding author: t.uysal@uq.edu.au

ABSTRACT

Australian terranes concealed beneath Mesozoic cover record complex Precambrian tectonic histories involving a successive development of several Proterozoic to Paleozoic orogenic systems. This study presents an integrated approach combining K–Ar, ^{40}Ar–^{39}Ar, and Rb–Sr geochronology of Precambrian authigenic illites from the recently discovered Millungera Basin in north-central Australia. Brittle deformation and repeated fault activity are evident from the sampled cores and their microstructures, probably associated with the large-scale faults inferred from interpretations of seismic survey. Rb–Sr isochron, ^{40}Ar–^{39}Ar total gas, and K–Ar ages are largely consistent indicating late Mesoproterozoic and early Proterozoic episodes (~1115 ± 26 Ma, ~1070 ± 25 Ma, ~1040 ± 24 Ma, ~1000 ± 23 Ma, and ~905 ± 21 Ma) of active tectonics in north-central Australia. K–Ar results show that illites from fault gouges and authigenic matrix illites in undeformed adjacent sandstones precipitated contemporaneously, indicating that advection of tectonically mobilised fluids extended into the undeformed wall rocks above or below the fracture and shear (fault gouge)

zones. Isotopic age data clearly indicates a Mesoproterzoic minimum age for the Millungera Basin and thus a previously unrecorded late Mesoproterozoic – early Neoproterozoic tectonic events in north-central Australia. This study provides insight into the enigmatic time-space distribution of Precambrian tectonic zones in central Australia, which are responsible for the formation of a number of sedimentary basins with significant energy and mineral resources.

Keywords: Fault gouge; illite; micro structure; fluid flow; isotope dating; Precambrian; Australia.

1. INTRODUCTION

Direct dating of brittle faulting is crucial for determining the absolute timing of inscrutable time-space distribution of tectonothermal events in concealed Precambrian terranes. Over the last decade, dating of illitic clay from near-surface fault gouges has increasingly become a routine approach to defining the timing of brittle deformations (van der Pluijm et al., 2001; Uysal et al., 2006; Mutlu et al., 2010; Zwingmann and Mancktelow, 2004, Zwingmann et al., 2010; Duvall et al., 2011; Hetzel et al., 2013, Torgersen et al., 2014; Mancktelow et al., 2016, Viola et al., 2016; Algea et al., 2019; Babaahmadi et al., 2019). This technique has been particularly useful in better understanding the development of convergent plate boundaries and continental collisions (e.g., van der Pluijm et al., 2001; Duvall et al., 2011; Isik et al., 2015; Algea et al., 2019; Babaahmadi et al. 2019), movements along transform plate margins (Uysal et al., 2006; Mutlu et al., 2009; Boles et al., 2015), and the formation of orocline bending accompanied by regional strike-slip faulting (Rosenbaum et al., 2015).

While fault gouges reported by earlier studies were mainly from surface outcrops, dating of concealed fault systems is more challenging due to the lack of direct structural observations. Although unknown fault systems buried under thick sedimentary basins can be denoted by geophysical techniques such 2D and 3D seismic reflections, cores from boreholes or tunnel sites intersecting fault zones can be used to date fault reactivation episodes (e.g., Viola et al., 2013; Yamasaki et al., 2013, Elminen et al., 2018). The current study investigates fault rocks and the host sandstone intersected in drill cores from the newly discovered Millungera Basin in north Queensland, north-central Australia (Fig. 1). It demonstrates how illite geochronology in combination with microstructural and mineralogical studies can be used to reveal a concealed, previously unrecorded Proterozoic tectonic events. Prior to this study (Fig. 1), almost no geological information was available on the Precambrian geology of large parts of north-central Australia, including the Millungera Basin, except for some regional geophysical data (Korsch et al., 2011, 2012) (Fig. 1). This is due to an extensive cover of sediments of the Jurassic–Cretaceous Eromanga-Carpentaria Basin (Fig. 1). Further uncertainties in tectonic interpretation of Australian Precambrian terranes arises from the tendency for original tectonic information to be masked by younger tectonics. Therefore, a major objective of this study was to provide insight into the enigmatic time-space distribution of Mid- to Late- Mesoproterozoic tectonic zones in central Australia, which are responsible for the formation of a number of sedimentary basins with significant potential for energy and mineral resources (Korsch et al., 2011, 2012).

Many previous studies have largely focussed on shallow crustal faults that form at diagenetic temperatures below 200°C. Fault gouges from such environments are assumed to consist of (1) detrital illite/muscovite ($2M_1$) derived from wall rocks and (2) authigenic or in situ illite ($1M/M_d$) precipitated within the brittle fault zone during faulting (van der Pluijm et al., 2001; Duvall et al., 2011). Based on a two-end member mixing model, quantified percentages of each illite polytypes (1M and $2M_1$) in different clay size fractions and their apparent $^{40}Ar–^{39}Ar$ ages are used to extrapolate the age of the pure authigenic illite-$1M/1M_d$ polytype (IAA: Illite Age Analyis approach, e.g., van der Pluijm et al., 2001; Duvall et al., 2011). However, assuming that $2M_1$ illite is systematically of detrital origin can be misleading, since the formation of authigenic $2M_1$ illite in diagenetic-to-hydrothermal conditions is also reported in the literature (e.g, Lonker and Gerald, 1990; Clauer and Liewig, 2013) and brittle faulting can produce authigenic 2M1 illite particularly in areas of elevated geothermal gradients or deeper parts of exhumed faults (Zwingmann et al., 2010; Viola et al., 2013; Mancktelow et al., 2015). While successful isotopic dating of brittle faulting within single fault core was reported previously (Viola et al., 2013), the present study integrating fault rocks from different depths and locations is a new and challenging approach to help better understand illite crystallisation in gouge during relatively low-temperature brittle fault reactivation episodes in complex Precambrian tectonic settings.

2. GEOLOGICAL SETTING, SAMPLE LOCATIONS AND SAMPLING

2.1. Regional tectonic history

The study area, the Millungera Basin is located in northwest Queensland, Australia (Fig. 1a). The Millungera Basin is surrounded by the Paleoproterozoic to Mesoproterozoic Mount Isa Province to the west and Neoproterozic – Ordovician Georgina Basin to the southwest, which developed along the eastern margin of the Proterozoic North Australian Craton. Proterozoic Australia comprises three main tectonic units including the North, West, and South Australian cratons. These units were independently accreted from older crustal fragments by ~1830 Ma (Myers et al., 1996). The North Australian craton has Archean and/or early Paleoproterozoic cores that has been superimposed by later Paleoproterozoic orogenic belts and basins (1800 – 1575 Ma) such as the Mount Isa and Etheridge provinces (Scott et al., 2000; Withnall et al., 2013) (Fig. 1a). The Mount Isa Province is a world-class mineralised terrain with large deposits of copper, lead and zinc, recording polyphase deformation and a multistaged metamorphism that affected the terrane during the Isan Orogeny between 1600 and 1500 Ma (O'Dea et al. 1997).

Australian continental fragments amalgamated as an early component of the Rodinean supercontinent between ~1300 Ma and 1100 Ma (de Vries et al., 2008; Li et al., 2008). The North Australian Craton was first joined to the northwestern margin of the West Australian Craton. The combined West and North Australian cratons were joined to the South Australia Craton along the Albany-Fraser Orogen. The Musgravian Orogen in central Australia was responsible for substantial crustal thickening and high-grade metamorphism at ~1200- 1150 Ma associated with granite intrusion (Evins et al., 2010; Kirkland et al., 2013). Thereafter, uplift and erosion were followed at ~1080 Ma by the deposition and of post-tectonic volcanism, accompanied by the intrusion of widespread plutons (Giles Complex) during the extension along the former collision zones (Schmidt et al., 2006; Evins et al., 2010; Aitken et al, 2013). At the same time, major swarms of dolerite intrusion (e.g., the Lakeview Dyke) were emplaced into the North Australian Craton in the Mount Isa Province (Tanaka and Idnurm, 1994).

During the Neoproterozoic an extensive intracratonic basin (Centralian Superbasin) developed over the junction between the North, South, and West Australian cratons. This was followed by the Rodinia breakup with a mantle plume that initiated continental rifting (Walter et al., 1995; Li et al., 1999). Rodinia breakup resulted in generation of a number of fault-bounded sedimentary basins. It has been proposed that initial period of extension occurred at about 900 Ma and was associated with igneous activities (e.g., Stuart dyke swarms, Black et al., 1980) and intracratonic basin formation in central-north Australia (e.g., Amedeus Basin, Korsch and Lindsay, 1989; Shaw et al., 1991). The Georgina Basin locating in close proximity to the Milungera Basin (Fig. 1a) represents another intarcratonic basin, which consists predominantly of Late Neoproterozoic, Cambro-Ordovician, and Devonian strata unconformably overlying Proterozoic crystalline basement (Shaw et al., 1991; Greene, 2010). The oldest sedimentary unit of the basin is considered to be ~825 Ma (Green, 2010 and references therein). The southern Georgina Basin was deformed during mid-Paleozoic Alice Springs Orogeny, whereby the Neoproterozoic normal faults of the rift basin were reactivated, which are now expressed as high-angle reverse faults (Green, 2010).

2.2. The Millungera Basin and sampling

The Millungera Basin is a recently discovered sedimentary basin in north Queensland, Australia (Korsch et al., 2011, Fig. 1a). It occurs to the east of the Paleoproterozoic Mount Isa Province and is covered by the thin Jurassic–Cretaceous Eromanga-Carpentaria Basin (Fig. 1b). An angular unconformity between the Eromanga and Millungera Basins indicates that the upper part of the Millungera Basin was eroded prior to deposition of the Eromanga-Carpentaria Basin (Korsch et al., 2011) (Fig. 1b), allowing sampling of the deeper part of the basin consisting of flat-lying to gently dipping sedimentary strata (Fig. 1b), which is strongly deformed and faulted (see below). A marked angular unconformity is also interpreted between the basement of the granite and metasedimentary basement rocks and the base of the Millungera Basin (Fig. 1b) Interpretation of gravity profiles indicates that the basin deepens to the south, with a possible maximum thickness of 4,000 m subsurface. Interpretation of aeromagnetic data suggests that the basin might have a dimension of up to 280 km by 95 km (Korsch et al., 2011). Apart from geophysical data, almost no geological information exists on the basin. Prominent thrust fault systems truncate both the western and eastern margins of the basin. Particularly the eastern part of the basin has been cut by several deep-penetrating, northeast-dipping thrust faults, with associated development of hanging wall anticlines. Based on SHRIMP U-Pb geochronology of detrital zircons from the Millungera Basin sandstones, the maximum depositional age of the Millungera Basin is constrained to 1574 ±

14 Ma (Neumann and Kositcin, 2011); however, it is a minimum age and not well constrained between the Cretaceous (overlying sediments) and Mesoproterozoic.

Core samples were taken from the lower parts of boreholes Julia Creek 1 (JC) and Dobbyn 2 (Dob) drilled as part of a state (Queensland)-wide geothermal investigation. The wells are 150 km apart (Fig. 1a and Table 1) and intersect the Mesozoic Eromanga-Carpentaria Basin in the upper part. Julia Creek 1 intersected 320.05m of the Eromanga Basin sequence and 179.97m of the Millungera Basin sequence; Dobbyn 2 intersected 332.40m of the Carpentaria Basin sequence and 155.64m of the Millungera Basin sequence. It should be noted that the succession within the Millungera Basin has not been formally defined. According to deep seismic reflection survey, a number of large-scale structures are interpreted to occur as basin-bonding and intra-basin fault systems (Fig 1a-b) (see Korsch et al., 2011). Small scale faults and fractures have also been described from logging of the cores extracted from JC and Dob (Faulkner et al., 2012; Fitzell et al., 2012). We collected a total of 9 Julia Creek 1 and 6 Dobbyn 2 fault gouge samples that were all analysed for the <2 μm clay mineral content (Table 1; Supplementary Fig. S1) and some of which have been selected for K–Ar, ^{40}Ar–^{39}Ar, and Rb–Sr dating and trace element studies. We also sampled representative host rock samples adjacent to the fault gouge zones (Table 1).

3. ANALYTICAL PROCEDURES

3.1. Clay characterisation

Samples were prepared for clay-fraction separation by gently hand-crushing the rocks to sand size to avoid artificially reducing grainsize of detrital/primary mineral components and then washed thoroughly by deionised water. Samples were then disaggregated in distilled water using an ultrasonic bath. Clay fractions were separated by the sedimentation method (for <2 μm) and centrifugation (for <1 μm subfractions to <0.1 μm). Oriented slides were prepared by pipetting the suspension onto a 30mm × 30mm glass slide to give a concentration of about 3 mg/cm^2 or more (Warr and Rice, 1994). XRD on whole-rock samples and clay separates of different size fractions were carried out (Table 1). The XRD analyses were conducted on a Bruker D4 Endeavor and D8 Advance (CoKα and CuKα radiation, respectively), operated at 40 kV and 30 mA at a scanning rate of 1°2θ/min and 0.05°/step. Following XRD analysis of air-dried samples, the oriented clay-aggregate mounts were placed in an ethylene–glycol atmosphere at 30–40°C overnight prior to additional XRD analyses. For polytype analyses, clay fractions of random powder from fault gouge samples (if sufficient amount of material was available) were scanned from 16 to 44 °2θ in the step-scanning mode with a step size of 0.05 degrees and a counting time of 30 second per step.

Illite polytypes for randomly oriented pure illite samples have been distinguished with the diagnostic peaks suggested by Grathoff and Moore (1996). To determine the $2M_1$ and $1M$ and $1M_d$ % contents of illite/muscovites, the ratios of (2.80 Å – 3.0 Å)/(2.58 Å) and (3.07 Å)/(2.58 Å) peak areas for $2M_1$ and $1M$, respectively were used, as proposed by Grathoff and Moore (1996). The presence of $1M_d$ illite was detected by the presence of the illite hump around the illite 003 diffraction peak (Grathoff and Moore, 1996). WINFIT decomposition by profile fitting was used for determination of areas of the specific peaks of polytypes. Polytype absolute quantification errors are estimated at about ±5%.

The Kübler index (KI) determinations, is defined as the width of the first order illite basal reflection (10Å peak) at half height (FWHM) and expressed in Δ2θ values. The Kübler index decreases with increasing illite crystallinity (a measure of the ordering/ thickness of illite crystallites), with temperature being the most important controlling factor (Ji and Browne, 2000 and references therein). KI is a well-accepted mineralogical indicator of anchizone, hydrothermal and low-temperature regional metamorphism and thermal conditions during fault activity (Merriman and Frey, 1999; Ji and Browne, 2000; Bense et al., 2014).

However, Arkai Index (AI) is becoming an additional or alternative technique (particularly in mafic rocks) to evaluate paleotemperature conditions (Árkai, 1991; Warr and Cox, 2016). The AI is determined through measurement of chlorite 002 peak width (Arkai, 1991). The KI and AI results of this study were calibrated against the Crystallinity Index Standard (CIS) scale using the procedure and interlaboratory standards of Warr and Mählmann (2015).

3.2. Petrographic analysis

The thin sections were first examined under plane-polarized light and cross-polarized light conditions using a Nikon Eclipse LV100N POL and a Zeiss Axio Imager.A2m polarizing microscope. Further examination of the thin sections was undertaken using a Philips XL 40 scanning electron microscope (SEM) equipped with a X-ray energy-dispersive spectrometry (EDS) system for chemical spot analyses. The sections were analysed using 30 kV accelerating voltage and a working distance of 12 mm. Images were collected in back-scattered electron mode. Additionally, clay separates were carbon coated and examined using an EDS equipped Zeiss Ultra Plus SEM qualitative phase identification. The samples were analysed under high vacuum with a 15 kV accelerating voltage and a working distance of 6 mm. Images of clay separate were collected in secondary electron acquisition mode.

3.3. Rb–Sr illite dating

For the Rb–Sr dating (conducted at the Radiogenic Isotope Facility laboratory RIF, the University of Queensland (UQ)), illitic clay separates were leached for 15 min at room temperature in 1 N distilled HCl (Clauer et al., 1993). Leachate and residue were separated by centrifuging. The residue was rinsed repeatedly with milli-Q water, dried and reweighed. Acid leached residues and untreated samples were measured directly by Thermo X-series 1 quadrupole ICP–MS with precision better than 0.5% (1σ). The Sr-enriched fraction was separated using cation exchange resins. Sr isotopic ratios were measured on a VG Sector-54 thermal ionisation mass spectrometer (TIMS. Sr was loaded in TaF_5 and 0.1 *N* H_3PO_4 on a tantalum or tungsten single filament. Sr isotopic ratios were corrected for mass discrimination using $^{86}Sr/^{88}Sr = 0.1194$. Long-term (6 years) reproducibility of statically measured NBS SRM 987 (2σ; n = 442) is $^{87}Sr/^{86}Sr = 0.710249 \pm 0.000028$. More recent dynamically measured SRM 987 had $^{86}Sr/^{88}Sr$ ratios of 0.710222 ± 0.000020 (2σ; n = 140). Rb–Sr isochron ages were calculated using the ISOPLOT program (Ludwig, 2012) and decay constant recomented by Villa et al. (2015). For isochron age calculation, standard errors of ±0.01% for $^{87}Sr/^{86}Sr$ and of ±1% for $^{87}Rb/^{86}Sr$ ratios were assigned to the results. Individual analytical uncertainties were generally smaller than these values.

3.4. K–Ar illite dating

The K–Ar dating was performed at the CSIRO Argon facility in Perth, Australia according to standard methods given in detail by Dalrymple and Lanphere (1969). Potassium content was determined by atomic absorption. The error of K determination of standards is better than 1.2% 1σ. The K blank was measured at 0.50 ppm. Argon was extracted from the separated mineral fraction by fusing the sample within a vacuum line serviced by an on-line ^{38}Ar spike pipette. The isotopic composition of the spiked Ar was measured with a high sensitivity, on-line, VG3600 mass spectrometer. The ^{38}Ar was calibrated against standard biotite GA1550 (McDougall and Roksandic, 1974). Blanks for the extraction line and mass spectrometer were systematically determined and the mass discrimination factor was determined periodically by airshots (small amounts of air for $^{40}Ar/^{36}Ar$ ratio measurement). During the course of the study, 16 international standards (8 HD-B1 and 8 LP-6) and 16 airshots were analyzed. The results are summarized in Table 2. The error for the $^{40}Ar/^{36}Ar$ value of the airshot yielded 296.08 ±1.23, (0.41%) 1σ. The general error for argon analyses is below 1.3% (1σ) based on the long-term precision of 330 measurements of international Argon standards. The K-Ar age was calculated using ^{40}K abundance and decay constants recommended by Steiger and Jäger (1977). The age uncertainties take into account the errors during sample weighing, $^{38}Ar/^{36}Ar$ and $^{40}Ar/^{38}Ar$ measurements and K analysis.

3.5. ^{40}Ar–^{39}Ar illite dating

Four fault gouge illites were dated by the ^{40}Ar–^{39}Ar method at the University of Michigan. Illitic clay samples were re-suspended in 1 ml of deionized water, spun-down at 10,000 rpm in a microcentrifuge and carved into a ~1 mm pellet following decanting. To avoid loss of ^{39}Ar due to recoil, clay pellets were placed in 1 mm ID fused silica vials prior to being sent for neutron irradiation for 90 MWh in medium flux locations of the McMaster Nuclear Reactor (hole 8C for irradiation 1, 8A for irradiation 2). Following irradiation, samples were attached to a laser fusion system, the vials were broken under a 1 x 10–8 Torr vacuum, and the samples step-heated in situ using a defocused beam from a 5 W Coherent Innova continuous Ar-ion laser operated in multi-line mode. Argon isotopes were then analyzed using a VG1200S mass spectrometer equipped with a Daly detector operated in analogue mode using methods by Hall (2014). Ages in this study are calculated relative to an age of 520.4±1.7 Ma for standard hornblende MMhb-1 (Samson and Alexander, 1987). The total gas age obtained from the vacuum encapsulated sample is equivalent to a conventional K–Ar age and quoted at 1σ.

3.6. Illite trace element analysis

For trace element analysis conducted in the Radiogenic Isotope Laboratory at the University of Queensland (RIF, UQ), clay samples were dissolved with a mixture of HF and nitric acids on a hotplate, then evaporated to dryness, refluxed twice with nitric acid and dissolved in 2N nitric acid. Aliquots of the solutions were spiked with internal standards, diluted and analysed on a Thermo X-series 1 quadrupole inductively coupled plasma mass spectrometer (ICP-MS). Sample preparation and analytical procedures used were similar to those of Eggins et al. (1997), except that Tm was not used as an internal standard and duplicate low-pressure digestions of US Geological Survey W-2 diabase standard and a known concentration profile (pre-analysed by laboratory) were used for calibration (Li et al., 2005). . The $^{156}CeO/^{140}Ce$ ratio for the run was 0.016. Long-term precision (RSD) was based on duplicate analyses of the duplicate digestions of AGV1, whilst precision for the run was based on five duplicate analyses of W-2 which were better than 3% for most elements, except for Li, Zn, Mo, Cd, and Cs, which ranged between 5% (Li, Cd and Cs) and 15% (Zn).

4. RESULTS

4.1 Sample description and micro structures

4.1.1 Core descriptions

The undifferentiated Millungera sequence intersected in Julia Creek 1 and Dobbyn 2 comprises medium to coarse-grained, pink to dark red quartzose sandstone with minor interbeds of micaceous clay siltstone and claystone. These sandstone intervals are fractured and faulted throughout the sequence and show evidence of pervasive hydrothermal alteration, particularly near the cracks (Fig. 2a, see also Faulkner et al., 2012; Fitzell et al., 2012). Alteration products are very fine-grained clay-rich material that contain angular clasts from the main rock (Fig. 2b). Clay-rich layers show mostly different colour (grey-beige-red) relative to the sandstone wallrock (Fig. 2b-e). Numerous open cracks coated with green clay are observed throughout cores (Fig. 2c). The clay rich material occurs along the fault planes and in cracks as single vein or complex network of partially consolidated material (Fig. c-d). They also exist as relatively thick layers (up to 30 cm) within the sandstone cores (Fig. 2e), with a sharp transition the host rock (Fig. 2a-f) and contain commonly slickenside surfaces at the contact with the host rock (Fig. 2f-h).

4.1.2 Petrographic and micro-structural analysis

Thin section photomicrographs and SEM images of representative samples are shown in Fig. 3a-f. Microscopic observations show that the undeformed host rock sandstones consist of mainly quartz, some muscovite and minor K-feldspar. Petrography, in combination with XRD analysis show that kaolinite, illite, and chlorite are present as a pore and fracture-filling cement in the sandstones (Fig. 3a-b), while detrital mica occurs in large elongate grains with alteration in illite along its edges (Fig. 3b-c). Chlorite does not show any coarse detrital grains and only occurs authigenetically in very fine-grains dispersed and mixed with illites as pore-filling mineral phases (Fig. 3a).

Faulted specimen from Julia Creek 1 show a characteristic S-C foliation (e.g. Berthe et al., 1979) under the optical microscope (Fig. 4a, b and c) with an anastomosing network of phyllosilicate defining the C shear oriented parallel to the shear direction. The S- shears include planes of insoluble minerals oriented oblique to the sense of shear (Fig. 4c) and quartz fragments embedded in a fine-grained illite-rich matrix as shown by electron microscopy imaging (Fig. 4d and e). These quartz grains have angular shape with intensely serrated grain boundaries and are slightly elongated with their long axis parallel to the orientation of the S- surface. Booklets of kaolinite partially replaced by illite are also visible in the deformed specimens (e.g. Fig. 4d and e).

Faulted hand specimens from Dobbyn 2 exhibit planar to slightly arcuate fault surfaces with a high gloss and display evident slickenside surfaces decorated by short-wavelength (200-500 μm) striations (Fig. 5a). Sense of shearing and offset on the faults are difficult to assess due to lack of markers visible in the cores. Domains of foliated and brecciated cataclasite can be distinguished on hand specimen (Fig. 5b) and in thin section (Fig. 5c). Both domains are characterised by hematite rich injection veins emanating from the slip surfaces and oriented at approximately right angle to them with sharp contacts with the surrounding material (Fig. 5 d, e). The domains are bounded by sharp contacts defined by slickenside surfaces constituted by thin layers (50-100 μm thick) of iso-oriented phyllosilicates (Fig. 5d, f). The foliated cataclasite domains are characterised by a set of conjugate shears referred to as S-C-C' structures visible at the micro-scale using scanning electron microscopy (Fig. 5e). Oblique to the shear direction S surfaces are defined by the preferred alignment of elongated phyllosilicate minerals and are oriented approximately perpendicular to the maximum flattening of the strain ellipsoid.

C and C' represent discrete shear surfaces, the former is parallel to the macroscopic slip surface and the latter deflects the S foliation by disrupting the grains into a plane composed of ultrafine comminuted grains oriented at a small angle (~ 20°) to the macroscopic shear surface but with the opposite sense of obliquity relative to the S-surfaces (Fig. 5e). The cataclasite domain show the original rock fabric of detrital quartz grains and pore-filling diagenetic kaolinite disrupted by a pervasive network of hematite filled intragranular micro-fractures (Fig. 5g).

4.1.3. XRD and SEM clay mineral analysis

Illite is the most abundant clay mineral in the majority of samples, with kaolinite and chlorite being present in many samples. The latter minerals are more abundant than illite in sample Dob-449.3 (Table 1; Supplementary Fig. S1). XRD analysis shows that 001 peak position of the illite does not change after ethylene glycol treatment, which indicates that smectite-like clays are not present or their amount is insignificant (Srodon and Eberl, 1984). There is also no noticeable change in KI values after the ethylene glycol treatment of the samples. KI measurements for <2 μm size fractions normalised to the standards of Warr and Rice (1994) range from 0.17 to 1.00 $\Delta°2\theta$ and from 0.46 to 1.01 $\Delta°2\theta$ for samples from Dobbyn 2 and Julia Creek 1, respectively (Table 1). We also measured KI values of >2 μm size fractions of some fault gouge samples. Such non-clay fractions contain mostly parallel-oriented mica-type inherited/detrital minerals representing the pre-fault protolith. Coarser (>2 μm) size fractions of samples JC-408, Dob-441, Dob-449.3, and Dob-476.6 KI give values of 0.42 $\Delta°2\theta$, 0.36 $\Delta°2\theta$, 0.14 $\Delta°2\theta$, and 0.26 $\Delta°2\theta$, respectively, whereas <2 μm fractions of the same samples provide considerably higher KI values of 0.60 $\Delta°2\theta$, 0.42 $\Delta°2\theta$, 0.19 $\Delta°2\theta$, and 0.33 $\Delta°2\theta$, respectively. KI values of < 2 μm size fractions of the host rock range between 0.18 and 0.23 $\Delta°2\theta$, and 0.46 and 0.68 $\Delta°2\theta$ for Dobbyn 2 and Julia Creek 1 samples, respectively (Table 1). The normalised chlorite crystallinity values (AI) of <2 μm for samples free of kaolinite range from 0.35 to 0.42 $\Delta°2\theta$ (Table 1).

Non-oriented random powder XRD analysis of <2 μm, 2-1 μm, <1 μm, and <0.5 μm fractions for samples from borehole Julia Creek 1 (JC) confirm the mixture of $2M_1$, 1M, and$1M_d$ polytypes of illite, while samples from borehole Dobbyn 2 consist of largely $2M_1$ illite with some $1M_d$ illite up to 20% for some samples (Table 1, Supplementary . S1). SEM analysis of <2 μm fractions show $2M_1$ illites forming large euhedral crystal plates with sharp edges that occur together with smaller $1M/1M_d$ illite plates (Fig. 3c-f). A number of previous studies (e.g., Clauer and Liewig, 2013) showed that detrital illitic clay particles rarely have straight edges, but rather occur in particles with diffuse-blurred and irregular edges (Fig. 3c, like the white material on the right-hand site). Samples Dob-441 and Dob-476.6 have generally larger crystal size (Fig. 3c-d) than samples JC-408 and JC-360.7 (Fig. 3c-d). The abundancy of $2M_1$ illite represented by these larger crystal plates in samples Dob-441 and Dob-476.6 is confirmed by XRD random powder polytype analysis (Table 1; Supplementary Fig. S1). Dob samples however, are poorly sorted in terms of crystal size distribution with the presence of a number of much smaller crystals (Fig. 3c-d). Such small crystals are mostly rounded (see the arrow in Fig. 3d).

4.2. Illite geochronology

4.2.1. ^{40}Ar–^{39}Ar dating

Four fault gouge illite samples of <2μm fraction were analysed for ^{40}Ar–^{39}Ar geochronology (Table 1 and Fig. 6). Based on their illite crystallinity values, these samples represent deep diagenetic to upper anchizonal metamorphic grade with 2M1 illite varying between 62% and 100%. Samples had 5%–12% low temperature ^{39}Ar recoil loss, which is characteristic of well crystallised illite grains (Hall et al., 1997). Age data (1σ) are obtained as total gas ages (Table 1 and Fig. 6) (cf., Dong et al., 1995). Samples JC-360.7, JC-408, Dob-441, and Dob-446.6 yield total gas of 1038.1 ± 2.9 Ma, 1040.0 ± 2.3 Ma, and 1068.1± 1.8 Ma, and 994.6 ± 2.2 (Table 1; Fig. 6). The analyses do not show well developed plateaux, which can be explained by recoil and varying ages of individual crystals (cf., Clauer et al., 2012).

4.2.2. K–Ar dating

K–Ar ages of fault gouge and sandstone illites of different size fractions from >2 μm to <0.1 μm from boreholes Julia Creek 1 and Dobbyn 2 are presented in Table 1 and Fig. 7. A histogram of all K–Ar results obtained from gouge zones are shown in Fig. 7a. K–Ar size fraction ages for fault gouge and host rock matrix illite and their interpretation in relation to the tectonic history are shown in Fig. 7b and Fig. 7c, respectively. Due to sample nature it was not possible to extract sufficient material for <0.1 μm or <0.5 μm fractions from some fault rock samples, especially from those samples from Dobbyn 2 with illites with low KI values (0.42 *Δ2θ* or lower for <2 μm).

Size fractions from <2 μm to <0.1 μm of fault gouge samples JC-343, JC-360.7, and JC-440.5 from Julia Creek 1 yield consistent ages (Table 1) with a mean (average) of 1036.2 ± 9.7 Ma, 1025 ± 17.7 Ma, 1028.9 ± 17.3 Ma (1 s.d.), respectively. The mean age of 1025 ± 17.7 Ma for sample JC-360.7 is identical with the Ar–Ar total gas age of 1038.1±2.9 Ma of <2 μm of the same sample. Various size fractions from 2-1 μm to <0.5 μm of another fault gouge sample from Julia Creek 1 (JC-408) give also consistent but older ages with a mean of 1114.2 ± 6.9 Ma. However, a younger ^{40}Ar–^{39}Ar total gas age of 1040.0 ± 2.3 Ma is obtained for <2 μm fraction of sample JC-408 (Table 1; Fig. 6). The >2 μm fraction of sample JC-408 yields, by contrast, a distinctively different and older K–Ar of 1243.2 ± 29.1 Ma (Table 1).

K–Ar ages of different fault gouge illites from Dobbyn 2 are more variable (Fig. 5a). 2-1 μm, <2, 1-0.5 μm, and 0.5-0.1 μm fractions of sample Dob-389.6 yield consistent ages (Table 1; Fig. 7b) with a mean of 1061 ± 19.5 Ma, whereas <0.5 μm and <0.1 μm give younger ages of 981.8 ± 22.6 Ma and 905.4 ± 20.9 Ma, respectively.

Smaller 2 and <1 μm fractions of fault sample Dob-441 give inconsistent but close K–Ar ages of 1148.7 ± 26.9 Ma and 1086.5 ± 25.1 Ma, respectively. The ^{40}Ar–^{39}Ar total gas age of 1068.1 ± 1.8 Ma for this sample is consistent with the K–Ar age of 1086.5 ± 25.1 Ma of the <1 μm fraction. A significantly older K–Ar age of 1312.3 ± 30.7 Ma is obtained for the >2 μm fraction of sample Dob-441 (Table 1; Fig. 7b).

Samples Dob-449.1 and Dob-449.3 were taken from a clay-rich fault rock zone, with the former and latter representing beige-light grey and hematite-rich red varieties, respectively. The 2-0.5 μm, <2 μm, 1-0.5 μm, and <0.5 μm fractions of sample Dob-449.1 yield younger but concordant ages with a mean of 922.4 ± 19.9 Ma. However, illite fractions of sample Dob-449.3 (just 20 cm below) yield scattering K–Ar ages regardless of the grain size. K–Ar ages of size fractions 2-1 μm, 1-0.5 μm, 0.5-0.2 μm, and <0.5 μm for sample

Dob-449.3 are 1047.7 ± 24.2 Ma, 1117.2 ± 25.8 Ma, 950.9 ± 22.0 Ma, and 1004.4 ± 23.2 Ma, respectively. Coarser > 2 μm fraction being rich in detrital mica gives a much older age of 1259.0 ± 29.1 (Table 1; Fig. 7b).

K–Ar age of 2-1 μm fraction and K–Ar and ^{40}Ar–^{39}Ar total gas ages of <2 μm fraction of the deepest fault rock sample from Dobbyn 2 (Dob-476.6) yield identical ages within analytical errors of 975.7 ± 22.2 Ma, 983.7 ± 23.0 Ma, and 994.6 ± 2.2 Ma, respectively, with a mean of 984.7 ± 9.5 Ma. A much older age of 1170.4 ± 27.4 Ma is obtained for >2 μm fraction of this sample (Table 1; Fig. 7b).

K–Ar and ^{40}Ar–^{39}Ar results of all size fractions (except >2 μm) from fault gouges listed in Table 1 are presented as a histogram and probability density distribution plot (Fig. 7a). Isotopic dates define distinct age clusters at ~1070 Ma, ~1040 Ma, and ~995Ma. There are also less pronounced, but noticeable age clusters at ~1115 Ma and ~905 Ma (Fig. 7a).

K–Ar ages of different size fractions of illitic clay minerals that occur as matrix in undeformed, adjacent sandstones (see Figs. 2 and 3) are also presented in Table 1 and Fig. 7c. Three different size fractions of three different samples, Dob-449.4, JC-500, and JC-360.6, yield same ages within error, averaging at 1047 ± 21 Ma, 1079 ± 13 Ma, 1062 ± 7 Ma (1 s.d), respectively (Table 1 and Fig. 7c). The <0.2 fine fractions of JC-360.6 and JC-500 yield within error identical younger agers of (928.3 ± 47.6 and 878.3 ± 45.1, respectively), which might indicate cessation of illite formation or partial reset due to final faulting with the Early Neoproterozoic deformation events and associated fluid flow.

4.2.3. Rb–Sr isochron dating

Rb–Sr data for the untreated, acid-leached residues, and leachates of different <2μm clay fractions for the fault gouge illites collected from different stratigraphic levels in Julia

Creek 1 and Dobbyn 2 are presented in Table 3 and on Fig. 8. The data show three parallel well-defined linear relationships indicating similar isochron ages, but with different initial $^{87}Sr/^{86}Sr$ values (Fig. 8a). Some samples plot between these lines (Fig. 8a), possibly because they have different initial $^{87}Sr/^{86}Sr$ values, and these samples are not considered for isochron age calculation. Samples from Dobbyn 2 plot on the two upper isochron lines with higher $^{87}Sr/^{86}Sr$ initial values (Fig. 8a). Residue of samples JC-360.7B<0.5 μm plot also on one of these lines (the middle line on Fig. Fig. 8a). All other Julia Creek 1 define a separate Rb–Sr isochron line with lower $^{87}Sr/^{86}Sr$ initial values (the lower line on Fig. 8a).

Leachates are accessory acid-soluble non-silicate phases (mostly carbonate minerals and amorphous grain coatings of FeO(OH) (Clauer et al., 1993). However, Rb–Sr isotopic systematics of the acid-soluble leachate is not in equilibrium with that of the illites, since the leachates plot off the Rb–Sr lines. Lower $^{87}Sr/^{86}Sr$ values of the leachates (mostly<0.72) in comparison to highly radiogenic (elevated) initial $^{87}Sr/^{86}Sr$ of of illites indicate interaction of rocks with some late stage fluids from which acid-soluble non-silicate phases were formed.

The data of untreated and residues of <2 μm fractions from Julia Creek 1 samples define a linear relationship from which the slope yields a Rb-Sr errorchron age of 1041 ± 46 Ma (initial $^{87}Sr/^{86}Sr = 0.7194 \pm 0.0011$, MSWD=27) (Fig. 8b). However, as apparent from the $^{87}Rb/^{86}Sr$ vs. $^{87}Sr/^{86}Sr$ plot on the Fig. 8a-b, untreated aliquots of samples JC-387.8 and JC-440.5 plot slightly at the lower part of the line leading to a large analytical error and MSWD value. This is probably caused by the effect of the leachable components that were not in isotopic equilibrium with the clays, as discussed above. When these two untreated samples are omitted, the data scatter is reduced significantly with a well-defined regression line (MSWD=2.3) and corresponding isochron age of 1023 ± 12 Ma (initial $^{87}Sr/^{86}Sr = 0.72009 \pm 0.00025$) (Figure 8c). Residue and untreated aliquots of <2 μm fractions from Dob-

449, Dob-441A, and Dob-389.6, and residue of JC-360.7B <0.5 μm yield an analytically indistinguishable age of 1033 ± 25 Ma (initial $^{87}Sr/^{86}Sr$ = 0.72326±0.00094; MSWD=2.5) (Fig. 8d). A somewhat younger Rb–Sr age of 1000 ± 12 (initial $^{87}Sr/^{86}Sr$ =0.72841±0.00030, MSWD = 0.065) was obtained for Dob-476.6 <2 μm (untreated and residue), Dob-389.6 2-1 μm and 0.5-0.1 μm (residue) (Fig. 8e).

4.3. Trace elements

Rare earth element (REE) data and Th, U, and Sc contents of illites (<2 μm clay-size fractions) from the fault gouge samples are given in Table 4. Chondrite-normalised REE patterns of illites from the fault gouges are shown in Fig. 9a. In addition, the REE pattern of Post-Archean Average Shale (PAAS, Taylor and McLennan, 1985) is included in the REE diagram. The fault gouge illites are substantially enriched in light REE (LREE) relative to PAAS with La contents as high as10xPAAS. The illites are however, somewhat depleted in heavy REE (HREE) relative to LREE (Fig. 9a). The chondrite-normalised $(La/Lu)_c$ ratios of the illites are significantly higher (up to 76) than the $(La/Lu)_c$ ratio of PAAS (10) (Table 4). Fault gouge illites are also enriched in Th and U (up to 10 times) in comparison to PAAS (Table 4).

5. DISCUSSION

5.1. Faulting, fluid-rock interactions and clay generation

Brittle deformation and faulting is evident from cores in the sampled intervals in Julia Creek 1and Dobbyn 2, probably associated with the large scale faults inferred from interpretations of seismic survey (Fig. 1). Under upper crustal conditions, fault zones accommodate intense shear strain often localised in bands of cataclastic deformation formed by friction-dominated faulting within the seismogenic regime (Sibson, 1977; Schmid and

Handy, 1991). While cataclastic fault rocks are generally considered to display random fabric, foliated fault rocks such as fault gouge and foliated cataclasites have also been reported in different lithologies ranging from crystalline rocks to siliciclastic and carbonate dominated sediments at different burial or deformation depths (Chester et al., 1985; Rutter et al., 1986; Lin, 1999; Ujiie et al., 2007; Laurich et al., 2004; Delle Piane et al., 2017; Nicchio et al., 2018). Frictional sliding and abrasion are common processes during repeated fault movement and result in strong grain size reduction of the fault rocks with respect to the constituting minerals in the undeformed portion of the host rocks. The abundant presence of micro and nano-sized particles in cataclasites and gouges may result from combined effects of cataclasis and pressure solution-precipitation during deformation in the presence of fluids (e.g. Vrolijk and van der Pluijm, 1999; Solum et al., 2005). Foliated cataclasites have also been observed at very shallow depths in siliciclastic sediments (<500 m, e.g., Balsamo et al., 2014) and carbonate rocks (< 2km; e.g., Smeraglia et al., 2016) as the result of cataclasis, clay smearing and/or pressure solution-precipitation in presence of fluids during deformation. The corroded grain boundaries of quartz grains in faulted samples from Julia Creek 1 (Fig. 4) and the presence of the injection veins and hydrothermal hematite in the cataclasites from Dobbyn 2 (Fig. 5) indicates that deformation occurred in a fluid-rich environment that promoted detrital muscovite dissolution and new growth of illite. The small injections veins that are observed to cut through the foliated cataclasites and the detrital quartz grains (Fig. 5) may represent the effect of hydraulic fracturing due to a fast increment of fluid pressure in the fault zone during a seismic slip (e.g. Sibson, 1989; Cowan et al., 2003; Ujiie et al., 2007; Rowe et al., 2012). At the core scale, some samples show no shearing-related fabrics in the sandstone cores (fresh and hard) adjacent to clay-filled cracks (Fig. 2a-d). This may be a result of the precipitation of clay-rich material and injection of granular material from seismically-mobilised circulating fluids (c.f., Smeraglia et al., 2016).

K–Ar results show that illites from fault gouges and matrix illites in undeformed adjacent sandstones precipitated contemporaneously (Fig. 7). In some tectonically active regions, mineral assemblages from the fault rocks and their parent rocks are significantly different, whereby parent rocks do not contain any alteration minerals with new mineral growth being restricted to the fault rocks. This indicates that the heat and fluid flows associated with mineral authigenesis were not controlled by regional tectonic events in these regions, but rather confined to the areas within the fault zone (e.g., Uysal et al. 2006; Isik et al., 2014; Babaahmadi et al., 2019). However, the relation between large-scale fluid flow and seismic events has long been reported (e.g., Bruhn et al., 1994; Eichhubl et al., 2010; Faulkner et al., 2010; Lupi et al., 2010 and references therein). Brittle faulting in the upper crust involves episodic changes in the stress level that can expel large volumes of fluids, leading to the generation of hydrothermal/geothermal systems (e.g., Maffucci et al., 2016). Faults and veins and their immediate surrounds represent zones of fluid passage and transfer of mass through those fluids (e.g., Sibson, 1987). Mineral alteration in slip zone gouge extends outward from the fault zone into the undeformed wall rock (e.g., Parry et al., 1991; Craw et al., 2009). The wall rock alteration is attributed to the diffusion and advection of fluids, and hence chemical mass and heat transfer associated with deformation. For example, metasomatic alteration zones develop around fluid pathways by advection with mineral dissolution and precipitation increasing towards the conduit and dictated by infiltrating fluids (Ferry and Dipple, 1991; Rossetti et al., 2011; Maffucci et al., 2016). Metasomatic mineral alteration is common in sedimentary basins contemporaneous with regional extensional tectonics. Alteration is driven by reactivity of sandstone host rocks with illitic clay minerals, K-feldspar (adularia), hematite, calcite, and quartz being some common minerals precipitating from tectonically mobilised K-bearing basin brine (Fedo et al., 1995; Michalski et al., 2007; Eichhubl et al., 2010, Rossetti et al., 2011). Similarly, in this study, sandstone immediately above or below the fracture and shear (fault gouge) zones represents zones of alteration of detrital minerals to illite by tectonically moved fluids.

5.2. Geochronology: comparison between K–Ar, ^{40}Ar–^{39}Ar and Rb–Sr ages

Fault gouges from the Millungera Basin in Australia (Fig. 1) contain a mixture of coevally formed $1M/1M_d$ and $2M_1$ illite from which the crystallisation age was determined by a combined application of Rb–Sr, ^{40}Ar–^{39}Ar, and K–Ar techniques. It is demonstrated that applying both the Rb–Sr and K–Ar (^{40}Ar–^{39}Ar) techniques for dating the same fault gouge minerals provides more robust and complementary age constraints on faulting episodes and minimises the inherent disadvantages for each isotopic system. A common drawback of Ar geochronology when dating white mica is that Ar apparent ages are either significantly older or younger than the Rb–Sr isochron ages of the same samples (Kelley, 2002; Di Vincenzo et al., 2006). Rb–Sr isotopic systematics may remain unaffected because Rb–Sr resetting requires higher closure temperatures and sufficient fluids in the system to facilitate recrystallisation (e.g., Di Vincenzo et al., 2006). However, a potential pitfall of Rb–Sr dating technique could result from heterogeneous initial $^{87}Sr/^{86}Sr$ ratios on a mineral-scale (cf., Davidson et al., 2005). In this study, as discussed in section in section 4.2.3, we minimised the effect of mineral-scale initial isotopic heterogeneity by analysing different aliquots (untreated, leachates, and residues) and different sub-size fractions of one clay sample. Indeed, different sub-size fractions and aliquots of some samples plot on different isochron lines indicating different $^{87}Sr/^{86}Sr$ ratios (Fig. 8, see the discussion below). Illites from the Millungera Basin fault gouges display well-developed linear data arrays on Rb–Sr isochron diagrams that we interpret to reflect statistically valid late Mesoproterozoic ages (Fig. 8).

Numerous case studies as discussed in detail below indicate that such linear relations can result from either a mixing between different mineral populations with different initial $^{87}Sr/^{86}Sr$ ratios, or from a complete isotopic equilibration of the entire mineral assemblage at a given time. In the former case, the linear relationship between $^{87}Rb/^{86}Sr$ and $^{87}Sr/^{86}Sr$ could have developed from a mixing line of two end members with potentially no genetic relationship, therefore without meaningful age information, whereas the latter relation provides a valid isochron whose slope yields the age of illitic clay generation during a fault reactivation event. However, valid and geologically significant isochrons and mixing lines can also be obtained simultaneously from samples with different mineral populations, comprising minerals with different Rb/Sr ratios but identical initial $^{87}Sr/^{86}Sr$ ratios. In this case of identical initial Sr-isotopic compositions of two components of a mixture at time t=0, the two components and mixtures thereof define a horizontal line both in a classic isochron diagram (which is the key condition for validity of calculated Rb–Sr isochron ages), and in the $^{87}Sr/^{86}Sr$ vs. $1/^{86}Sr$ diagram commonly used for evaluation of binary isotopic and compositional mixing (cf. Wendt, 1993 and Schneider et al. 2003 for theoretical background). In sedimentary basins or hydrothermal systems, samples with various Rb/Sr ratios can precipitate from a chemically homogeneous basinal fluid that can yield the same isotopic composition across the entire sedimentary basin (e.g., Uysal et al., 2001; Golding et al., 2013). Fault gouge clay separates from the Milungera Basin contain a mixture of illites and other authigenic clay minerals such as chlorite and kaolinite (see the section 4.1.2) and minor carbonates, which include considerable amounts of Sr but no or very little Rb (in contrast to illite). Since samples used for Rb–Sr analysis contain these different minerals in various amounts, the obtained linear relations can be considered to have evolved from (initially horizontal) mixing lines but simultaneously represent geologically meaningful isochron correlations. The isochron ages are consistent with K–Ar ages of the same clay-size fractions of the corresponding samples that provides a further strong support in favour of isochrons with a meaningful age information (see below). Similarly, valid Rb–Sr ages based on linear relations representing both isochrons and mixing lines were commonly obtained from leachate, untreated, and residue aliquots of fault gouge and matrix illites (Clauer and Chaudhuri, 1995; Mutlu et al., 2010; Uysal et al., 2011; Golding et al., 2013; Isik et al., 2014; Middleton et al., 2014; Rosenbaum et al., 2015; Babaahmedi et al., 2019).

The Rb–Sr isochron ages of JC samples are concordant with K–Ar ages of same samples (Table 1). For example, the Rb–Sr isochron ages (1041 ± 46 Ma and 1023 ± 12 Ma) for <2 μm fractions of samples JC-360.7, JC-440.5 (Fig. 8b-c) are consistent with K–Ar and for $^{40}Ar–^{39}Ar$ (sample JC-360.7) ages of the same fraction and all other different size fractions of the same samples (Table 1 and Fig. 7). However, K–Ar and Rb–Sr ages are not consistent for a number of Dob samples. K–Ar ages of Dob-389.6 and Dob-441samples are older than the corresponding Rb–Sr isochron ages, while K–Ar ages of all different size fractions for sample Dob-449.1 are lower (925 to 913 Ma) than the Rb–Sr isochron age (Fig. 8b-d, Table 1). The Rb–Sr isochron age of 1000 ± 12 Ma for <2 μm of sample Dob-476.6 (along with the acid-leached residues of Dob-441B and Dob-389.6 for 2-0.5 μm to 0.5-0.1 μm fractions) is consistent with K–Ar ages of the same sample for coarser size fractions (975.7 ± 22.2 and 983.7 ± 23.0 Ma) within analytical errors. <1 μm fraction of sample Dob-476.6 yields a consistent K–Ar age (922.2 ± 21.2) with clays of all size fractions of sample Dob-449.1 (Table 1).

In summary, all JC samples with their various size fractions yield consistent Rb–Sr isochron and individual K–Ar ages. This finding is similar to those reported by some recent studies that presented robust and comprehensive Rb–Sr, $^{40}Ar–^{39}Ar$, and K–Ar age data for deep diagenetic and anchizonal fault gauge illites (e.g., Middleton et al., 2014; Rosenbaum et al., 2015; Babaahmadi et al, 2019). Discrepancy in Rb–Sr and K–Ar ages for Dob samples, e.g., Dob-441 <2 μm (K–Ar age is older) and Dob-449.1 (K–Ar ages are younger), and the internal inconsistency of K–Ar ages among different size fractions of sample Dob-4449.3

(e.g., 1048 ± 24 for 2-1μm and 1117 ± 26 for 1-0.5 μm fractions; see Table 1) may result from sample heterogeneity (hand-specimen and micro scale, see Figs. 4 and 5) presented by more than one illite generation due to multiple faulting episodes (see section 5.4).

Mixing of different generations is possible in small scale as a result of variable degrees of isotopic resetting of a single illite generation during subsequent faulting events. Pervasive overprinting and re-crystallization can be hindered even in micro scale, which may result from a lack of permeability and/or limited availability of fluids (e.g., Bröcker et al., 2013).

5.3. Implication of Sr isotope and trace element compositions for the evolution of fault-related fluids

The trace element composition of authigenic clay minerals reflects the mineral/fluid partition coefficients for different elements, as well as the composition of fluids from which the clays precipitated. Trace element contents and concentrations, as well as some element ratios, can be used to trace the origin of basinal and hydrothermal fluids (e.g., Uysal and Golding, 2003; Uysal et al., 2005; Uysal et al., 2011). The fault gouge illites analysed in this study are highly enriched in LREE and other incompatible elements such as Th and U relative to PAAS (Fig. 9a and Table 4). This geochemical characteristic indicates precipitation of the illites from fluids that must have interacted with rocks of the upper crust enriched in incompatible and heat producing elements. This is also consistent with initial $^{87}Sr/^{86}Sr$ values of fault gouge illites that reflect Sr isotope composition of fluids from which the illites precipitated. The radiogenic initial $^{87}Sr/^{86}Sr$ ratios of about 0.72 indicate the involvement of fluids that equilibrated with old Rb-rich crustal rocks. The trace element and Sr isotope data are in agreement with seismic and potential field data by Korsch et al. (2011), which is interpreted as indicating the occurrence of granites with a thickness of up to 5.5 km below the Millungera Basin. The inferred granites may be a part of the granite (Williams

Supersuite) exposed just to the west in the Mt Isa Inlier, which is enriched in Th, U, and K (Korsch et al., 2011 and references therein).

Different $^{87}Sr/^{86}Sr$ initial values of illites of the parallel isochron lines corresponding to the same Rb–Sr age in Fig. 8 and scatter of Rb–Sr data points for some samples indicate separate circulation pathways for seismically mobilised fluids that that might have restricted to unconnected fault planes and fracture systems in different areas of the Millingera Basin.

5.4. Changes of illite crystallinity in relation to K–Ar ages

A valid interpretation of illite isotopic ages in relation to deformation history is subject to a solid mineralogical characterisation of samples. Particularly, information about the illite crystallinity and illite polytype data are critical in assessing the illite crystallisation temperature and a possible contamination of samples by metamorphic detrital muscovite from the undeformed host rock. Illite crystallinity is commonly used to identify the transitional anchimetamorphic zone between the diagenesis and epimetamorphic zone of low-grade metamorphism. The boundary limit from diagenetic to anchimetamorpic conditions has been reported to be at 0.52°2θ, whereas the anchizone-epizone boundary is set at 0.25°Δ2θ (Warr and Mählmann, 2015). Accordinly, KI values of <2 and 2-1 Julia Creek illitic clays indicate diagenetic and anchizone metamorphic conditions. Since these illites occur as a discrete phase (containing no expandable layers) and contain both $1M/M_1$ and $2M_1$ polytypes they indicate formation temperatures of about 200ºC and higher (cf., Hoffman and Hower, 1979, Walker and Thompson, 1990). Although the $2M_1$ polytype has been known to appear usually at temperatures higher than 250°C (Srodon and Eberl, 1984), its occurrence at lower temperatures at about 200-250°C in co-existence with $1M/M_d$ has also been reported (Walker and Thomson, 1990, Chen and Wang, 2007; Hejing et al., 2008). KI values show considerable differences between samples from Julia Creek and Dobbyn areas (Fig. 10), which clearly indicate different paleothermal conditions in different areas. <2 μm fractions of Julia Creek fault gouge samples show similar KI values with insignificant changes with depth, except a spike for the sample at 440.5 m (Fig. 10). Samples from Dobbyn 2 are characterised by lower KI values and the dominance of $2M_1$ illite (Fig. 10, Table 1).

Our interpretation of the significance of K–Ar ages for fault gouge and matrix illite is based on K–Ar age versus grain size and KI relationships (Fig. 7b and Fig. 11a, b, c). This relationship can represent either an inclined or a parallel age spectrum. The parallel age spectrum results from identical K–Ar ages of different size fractions within error, representing internal consistency, which is regarded as geologically meaningful (e.g., Clauer and Chaudhuri, 1995; Torgersen et al., 2014; Vialo et al., 2016). The inclined age spectrum can arise from the presence of multiple illite generations, such as either an earlier authigenic illite generation or inherited (detrital) components mixing with younger authigenic illites. The slope of the spectrum is a function of the age difference between the two age end members.

Plotting KI values vs. K–Ar ages, fault gouge samples from Julia Creek 1 indicate almost flat spectrums with identical (within error) or slightly decreasing ages between 1049 ± 25 and 1006 ± 23 Ma for most of the JC samples and at ~1100 Ma for sample JC-408) (Fig. 11a). These concordant K–Ar ages of samples with changing grain size (Fig 7b) and KI values can those be considered as meaningful as indicating the timing of major deformation events. Similarly, an age clustering around 1060 Ma of samples with changing grain sizes and KI values is evident for matrix illites (Fig. 7c and Fig. 11c).

There are two different KI values vs K–Ar age populations of Dobbyn 2 fault gouges, displayed by the shallow (above 441 m) and deeper (below 441 m) samples, which are distinguished by higher and lower KI values, respectively. They show two parallel trends with reasonably well negative correlations (Fig. 11a), which may be considered as mixing of two possible end members. These may be represented by an earlier illite generation at ~1100

Ma (similar age as various size fractions of sample JC-408, see above) and a later illitization or isotopic resetting at ~900 Ma. The correlations in Fig. 11b can also be interpreted as indicating the effect of numerous and superimposed slip episodes during discrete faulting events. A similar K–Ar age range but different extend for KI values of Dobbyn 2 fault gouges indicate that different thermal conditions prevailed in the shallower and deeper parts (see the discussion above for the illite crystallinity) occurred in the same time period. Although decreasing K–Ar ages with increasing KI values of Dob samples could be due to decreasing amount of detrital illite/muscovite with decreasing grain size, K–Ar ages for different size fractions and KI values of sample Dob-389.6 (2-1, <2, 1-0.5, and 0.5.0.1μm), Dob-449.1 (2-0.5, <2, 1-0.5,and <0.5μm), and Dob-476.6 (2-1and <2μm) are consistent within analytical error. This, together with authigenic mineral textures of illites (Fig. 3), suggests that the presence of detrital muscovite in <2 fractions is unlikely.

Lowest K–Ar ages associated with highest KI values indicate later recrystallisation of illites in finer crystals or isotopic resetting of finer illites at relatively lower temperatures not affecting the coarser size fractions. Thermally activated volume diffusion in clay minerals leading to ^{40}Ar loss can cause decreasing K–Ar ages with decreasing grain sizes of clays (e.g., Torgersen et al., 2014; Lerman, et al., 2007). The finest clay size fractions are more susceptive to younger thermal events due to poor radiogenic argon retentivity because of smaller diffusion radius and less crystallinity. Consequently, re-heating of earlier formed finest particles during a later thermal event to a temperature high enough to enable ^{40}Ar diffusion from the crystal structure could cause partial or complete resetting of the K–Ar isotopic systematics (Clauer and Chaudhuri, 1999). Alternatively, the finest fraction represents the last clay growth of newly crystallised tiny illite crystallites, which can occur during fluid flow events related to tectonically active regimes (e.g., Zwingmann and Mancktelow, 2004; Uysal et al., 2006). The size of authigenic clay minerals can be a function of both the duration of crystal growth and the crystallisation temperature (Frey, 1987; Cashman and Ferry, 1988). The ages of the finest grain size fractions therefore date either the timing of the last, short-lived thermal and/or fluid flow events (c.f., Torgersen et al., 2015) or cooling events after a prolonged burial and mineral growth, which took place in Neoproterozoic latest.

5.5. Significance for regional tectonics

Northeast Australia lies on a cratonic margin that has had a complex crustal history involving the successive development of several Proterozoic to Paleozoic orogenic systems (Fig. 12). Age data from the faults defining the margins of the Millungera Basin is thus important in revealing concealed major Proterozoic tectonic zones in Australia, which contain energy and mineral resources (Korsch et al., 2011). The age data from the fault gouges provide clear evidence for a late Mesoproterozoic minimum age for the Millungera Basin, and are in accordance with the early-mid Mesoproterozoic maximum depositional age of the Millungera Basin as constrained from zircon ages for Millungera Basin sandstones (Neumann and Kositcin, 2011).

The fault gouge ages clustering at (~1115 ± 26 Ma, ~1070 ± 25 Ma, ~1040 ± 24 Ma, ~1000 ± 23 Ma, and ~905 ± 21 Ma (Fig. 7) may be related to the regional extension and associated major thermal event that occurred across Australia at 1120-900 Ma (e.g., Musgrave Orogeny and subsequent Giles Event), due to interactions between Australia and other continents during assembly of the supercontinent Rodinia (De Vries et al., 2008; Li et al., 2008; Evins et al., 2010). This Australia-wide tectono-thermal event that largely developed along former (Mesoproterozoic) collision zones led to emplacement of widespread dyke swarms, sills and associated granite plutons in the central and north Australia craton largely in a time frame between ~1040 Ma and ~1090 Ma (Schmidt et al., 2006; Evins et al., 2010; Aitken et al., 2013). The Musgrave Orogeny involving widespread emplacement of granite and mafic–ultramafic bodies were recorded in central Australia at 1220 Ma and 1120 Ma (Evins et al., 2010; Kirkland et al., 2013). Major swarms of dolerite intrusions in the North Australian Craton dated at 1116±12 Ma (Lakeview Dolerite, Tanaka and Idnurm, 1994) and associated hydrothermal events were recorded in the Mt. Isa Province (adjacent to the study area, Fig. 1) (Uysal et al., 2004). The illite ages clustering around ~1100 Ma coincide with the latest stage of the Musgrave Orogeny Fig. 7b, Fig. 12).

Another cycle of mafic intrusions in central Australia occurred during the extensional Giles Event between ~1078 Ma and 1068 Ma (Evins et al., 2010; Aitken et al., 2013 and references therein), which was followed by granite magmatism and accompanied felsic volcanism between ~1050 Ma and ~1040 Ma (Evins et al., 2010 and references therein). The latest phase of the Giles Event is represented by the felsic Smoke Hill Volcanics yielding a age of 1026±26 Ma. The K–Ar ages clustering around ~1040 Ma of different illite size fractions from the fault gouges and sandstones are consistent with the timing of the later stage of the Giles event.

Orogenic events post-dating the Giles event are represented by mafic dykes and rare pegmatites emplaced at about 1000 Ma (Evins et al., 2010). Further, a Rb–Sr age of 897 ± 9 Ma is reported for dolerite from the Stuart Dyke Swarm in the southern part of the Arunta Block, Northern Territory (Black et al., 1980). The Rodinia supercontinent assembled through worldwide orogenic events by 900 Ma. Stresses induced by the ca. 900 Ma event probably caused reactivation of older orogens within Rodinia (Li et al., 2008). The Amadeus Basin in north central Australia was initiated at ~900 Ma in the late Proterozoic by crustal extension, probably in associations with mafic intrusions being correlated with the Stuart Dyke Swarm (Korsch and Lindsay, 1989). Fault gouge K–Ar ages of ~900 – 950 Ma for various size fractions from sample Dob-449.1 and finest fraction (<0.1 mm) from Dob-389.6 coincide with the timing of deformation associated with these early Neoproterozoic igneous and deformation events (Fig. 7b).

The dated faults of the Millungera Basin may be associated regionally with a series of fault systems bounding rift basins in the southern Georgina Basin. Those fault zones (e.g., Burke River Structural Belt, Pilgrim Fault Zone, Greene, 2010), which are in close proximity to and run parallel to the dated faults framing the Millungera Basin, occur extensively in the adjacent Mt Isa Inlier (Greene, 2010; Korsch et al., 2011). The Pilgrim Fault Zone was established a Mesoproterozoic structural boundary within the Mt. Isa Inlier (Greene, 2010). The southern Burke River Fault, just to the west of the Millungera Basin (Fig. 1), represents a rift-bounding normal fault, were reactivated and inverted to reverse faults during the mid-Paleozoic Alice Springs Orogeny (~400-350 Ma) (Greene, 2010). Similarly, samples from this study were taken from thrust faults at the margin of the Milungera Basin. However, the K–Ar, ^{40}Ar–^{39}Ar, and Rb–Sr ages of the fault gouge illites have been essentially preserved and no tectonic event after about 905 Ma has reset the isotopic systematics of these fault gouges (Fig. 12). This can be explained by the lack of significant fluid or heat flow events allowing recrystallisation or ^{40}Ar diffusion from illites. In conclusion, our geochronological age data constrain the timing of fault activity associated with the late Meseproterozoic and early Neoproterozoic emplacement of the intrusions and crustal regional extension in central-north Australia.

6. CONCLUSIONS

A new integrated study was conducted employing radiometric age dating (K–Ar, ^{40}Ar–^{39}Ar, and Rb–Sr) of illitic clay minerals from fault gouges and Neoproterozoic host sandstones bounding the recently discovered Millungera Basin in north-central Australia. Rb–Sr isochron, ^{40}Ar–^{39}Ar total gas, and K–Ar ages are consistent indicating late Mesoproterozoic and early Proterozoic episodes (~1115 ± 26 Ma, ~1070 ± 25 Ma, ~1040 ± 24 Ma, ~1000 ± 23 Ma, and ~905 ± 21 Ma) of active tectonics in north-central Australia. These faulting episodes correspond to timing of regional extension and associated major thermal event that occurred across Australia at 1120-900 Ma, due to interactions between Australia and other continents during assembly of the supercontinent Rodinia. Sr isotope and trace element data indicate that fault gouge illites precipitated from fluids that interacted with deep granitic basement enriched in heat-producing elements. This study provides insight into the inscrutable time-space distribution of Precambrian tectonic zones in central Australia, which are responsible for the formation of a number of sedimentary basins with significant energy and mineral resources. Investigating core samples with preserved isotopic signature of Proterozoic fault rocks avoids the effect of surface weathering of old geological terranes.

Acknowledgements

Support for this research was provided by Queensland Geothermal Energy Centre of Excellence (QGECE) funded by the Queensland State Government. Support by Hal Gurgenci (former QGECE's director) is particularly acknowledged. The manuscript benefited from comments by Tony Allan who is greatly appreciated. Espen Torgersen and Neil Mancktelow are gratefully acknowledged for their very useful and constructive comments of an earlier version of the paper, which helped significantly to improve the manuscript. Furthermore, comprehensive reviews by Luca Aldega and Roelant van der Lelij and their constructive comments and suggestions have greatly improved the manuscript. Michael Verrall is thanked for his assistance for the SEM work. We thank Yue-xing Feng and Ai Duc Nguyen for their help with analytical work and technical assistance to perform Rb–Sr and trace-element analyses. We thank Turgay Demir for his assistance during sample preparation, and we particularly acknowledge Chris Hall for his great help in undertaking the $^{40}Ar/^{39}Ar$ analysis at the University of Michigan. We thank Norbert Clauer and Johannes Glodny for discussions of the geochronological data. The Geological Survey of Queensland is particularly acknowledged for providing access to core sampling.

References

Aitken A. R. A., Smithies R. H, M. C. Dentith, A. Joly, S. Evans and Howard H. M. (2013) Magmatism-dominated intracontinental rifting in the Mesoproterozoic: The Ngaanyatjarra Rift, central Australia. *Gondwana Res.*, 24, 886-901.

Algea, L. Viola, G., Casas-Sainz, A., Marcén, M., Román-Berdiel, van der Lelij. (2019) Unraveling multiple thermo-tectonic events accom- modated by crustal-scale faults in northern Iberia, Spain: Insights from K-Ar dating of clay gouges. *Tectonics*, **38**, 3629-3651.

Árkai P. (1991) Chlorite crystallinity: an empirical approach and correlation with illite crystallinity, coal rank and mineral facies as exemplified by Palaeozoic and Mesozoic rocks of northeast Hungary. J. *Metamorph. Geol.* **9**, 723–734.

Babaahmadi, A., Uysal, I.T., Rosenbaum, G. (2019). Late Jurassic intraplate faulting in eastern Australia: a link to subduction in eastern Gondwana and plate tectonic reorganisation. *Gondwana Research*, **66**, 1-12.

Balsamo, F., Aldega, L., De Paola, N., Faoro, I., Storti, F. (2014). The signature and mechanics of earthquake ruptures along shallow creeping faults in poorly lithified sediments., *Geology*., **42**, 435-438.

Bense, F.A., Wemmer, K., Löbens, S. Siegesmund, S. (2014). Fault gouge analyses: K-Ar illite dating, clay mineralogy and tectonic significance—a study from the Sierras Pampeanas, Argentina. *International Journal of Earth Sciences*, **103**, 189-218.

Berthé D., Choukroune P. and Jégouzo, P. (1979) Orthogneiss, mylonite and non coaxial deformation of granites: the example of the South Armorican Shear Zone. *J. Struct. Geol*. **1**, 31-42.

Black L.P., Shaw R.D. and Offe, L.A. (1980) The age of the Stuart Dyke Swarm and its bearing on the onset of late Precambrian sedimentation in central Australia. J. Soc. Austr., 27, 151-155.

Boles A., van der Pluijm B., Mulch A., Mutlu H., Uysal I.T. and Warr, L. (2015) Hydrogen and 40Ar/39Ar isotope evidence for multiple and protracted paleofluid flow events within the long-lived North Anatolian Keirogen (Turkey). *Geochem. Geophy. Geosy*. **16**, 1975-1987.

Bröcker, M., Baldwin, S., Arkudas, R. (2013). The geological significance of ^{40}Ar/^{39}Ar and Rb–Sr white mica ages from Syros and Sifnos, Greece: a record of continuous (re)crystallization during exhumation? *J. Metamorph. Geol*. **31**, 629–646.

Chen, T. and Wang, H.J. (2007). Determination of layer stacking microstructures and intralayer transition of illite polytypes by high-resolution transmission electron microscopy (HRTEM). *American Mineralogist*, **92**, 926-932.

Chester F.M., Friedman M. and Logan, J.M. (1985) Foliated cataclasites. *Tectonophysics* **111**, 139-146.

Clauer, N. and Chaudhuri, S., 1995. Clays in Crustal Environments. Isotope Dating and Tracing. Springer Verlag, Heidelberg, 359 p.

Clauer N., Chaudhuri S. Kralik S. and Bonnotcourtois C. (1993) Effects of experimental leaching on Rb-Sr and K-Ar isotopic systems and REE contents of diagenetic illite, *Chem. Geol.* **103**, 1-16.

Clauer N., Zwingmann H., Liewig N. and Wendling R. (2012) Comparative 40Ar/39Ar and K-Ar dating of illite-type clay minerals: a tentative explanation for age identities and differences. *Earth-Sci. Rev*. 115, 76–96.

Clauer, N. and Liewig, N. (2013) Episodic and simultaneous illitization in oil-bearing Brent Group and Fulmar Formation sandstones from the northern and southern North Sea based on illite K–Ar dating. *Am. Assoc. Pet. Geol. Bull.* **97**, 2149–2171.

Craw, D., Upton, P. and Mackenzie, D.J. (2009). Hydrothermal alteration styles in ancient and modern orogenic gold deposits, New Zealand. *New Zealand Journal of Geology and Geophysics*, **52**, 11-26.

Dalrymple G.B. and Lanphere, M.A. (1969) Potassium-argon dating. W.H. Freeman, San Francisco, 258 p.

Davidson, J., Charlier, B., M.H., Perlroth, R. (2005). Mineral isochrons and isotopic fingerprinting: Pitfalls and promises. *Geology*, **33**, 29–32.

de Vries S.T., Pryer L.L. and Fry N. (2008) Evolution of Neoarchaean and Proterozoic basins of Australia. Precambr. Res., **166**, 39–53.

Delle Piane C., Clennell M.B., Keller J.V., Giwelli A. and Luzin, V. (2017) Carbonate hosted fault rocks: A review of structural and microstructural characteristic with implications for seismicity in the upper crust. *J. Struct. Geol.* **103**, 17-36.

Di Vincenzo G, Tonarini S, Lombardo B, Castelli D and Ottolini L. (2006) Comparison of 40Ar/39Ar and Rb-Sr data on phengites from the UHP Brossasco-Isasca unit (Dora Maira Massif, Italy): implications for dating white Mica. *J. Petrol.* **47**, 1439–1465.

Duvall A.R., Clark M.K., van der Pluijm B.A. and Li C. (2011) Direct dating of Eocene reverse faulting in northeastern Tibet using Ar-dating of fault clays and low-temperature thermochronometry. *Earth Planet. Sci. Lett.* **304**, 520-526.

Eberl, D.D., Środoń, J., Kralik, M., Taylor, B.E, and Peterman, Z.E., 1990. Ostwald ripening of clays and metamorphic minerals, Science 248, 474–477.

Eggins S.M., Woodhead J.D., Kinsley L.P.J., Mortimer G.E., Sylvester P., McCulloch M.T., Hergt J.M. and Handler M.R. (1997) A simple method for the precise determination of >=40 trace elements in geological samples by ICPMS using enriched isotope internal standardization. *Chem. Geol.* **134**, 311-326.

Eichhubl, P., Davatzes, N.C., and Becker, S.P. (2010). Structural and diagenetic control of fluid migration and cementation along the Moab fault, Utah. AAPG Bulletin, 93, 653-681.

Elminen T., Zwingman, H. and Kaakinen A. (2018) Timing of brittle deformation and sedimentation within the Savio tunnel site, Southern Finland – Implication for sediment sources in Fennoscandia. – Precambrian Research, 304, 110-124, doi.org/10.1016/j.precamres.2017.10.014

Evins P.M., Smithies R.H., Howard H.M., Kirkland C.L., Wingate M.T.D. and Bodorkos S. (2010) Redefining the Giles Event within the setting of the 1120–1020 Ma Ngaanyatjarra Rift, west Musgrave Province, Central Australia. *Geological Survey of Western Australia, Record* 2010/6, 36p.

Faulkner, D. R., Jackson, C. A. L., Lunn, R. J., Schlische, R. W., Shipton, Z. K., Wibberley, C. A. J., and Withjack, M. O. (2010). A review of recent developments concerning the structure, mechanics and fluid flow properties of fault zones. Journal of Structural Geology 32, 1557–1575.

Faulkner S.P., Maxwell M., O'connor L.K., Sargent S.N., and Talebi B. (2012) Coastal Geothermal Energy Initiative GSQ Julia Creek 1: well completion report and heat flow modelling results. *Queensland Geological Record* 2012/05.

Fedo, C.M., Nesbitt, H.W., Young and G.M. (1995). Unraveling the effects of potassium metasomatism in sedimentary rocks and paleosols, with implications for paleoweathering conditions and provenance. *Geology*, **23**, 21–924.

Frey, M. (1987). Very-low-grade metamorphism of clastic sedimentary rocks. In: Low temperature Metamorphism, M. Frey, editor. Blackie and Son, Glasgow. 351 pp.

Ferry, J.M. and Dipple, G.M. (1991). Fluid flow, mineral reactions, and metasomatism. *Geology*, **19**, 211-214.

Fitzell M.J., Maxwell M., O'connor L.K., Sargent S.N. and Talebi B. (2012) Coastal Geothermal Energy Initiative, GSQ Dobbyn 2 Well completion report and heat flow modelling results. *Queensland Geological Record* 2012/04.

Golding, S.D., Uysal, I.T., Bolhar, R., Boreham, C.J. Dawson, G.K.W., Baublys, K.A., and Esterle, J.S. (2013). Carbon dioxide-rich coals of the Oaky Creek area, central Bowen Basin: a natural analogue for carbon sequestration in coal systems. *Australian Journal of Earth Sciences*, **60**, 125-140.

Grathoff G.H. and Moore D.M. (1996) Illite polytype quantification using Wildfire© calculated X-ray diffraction patterns. *Clay. Clay Miner.* (44) 835–842.

Greene, D.C. (2010) Neoproterozoic rifting in the southern Georgina Basin, central Australia: Implications for reconstructing Australia in Rodinia. *Tectonics* **29**, TC5010, doi:10.1029/2009TC002543.

Hall C. M. (2014) Direct measurement of recoil effects on ^{39}Ar-^{40}Ar standards. *Geol. Soc. London Spec. Publ.*, **378**, 53-62.

Hall C. M., Higueras P. L., Kesler S. E., Lunar R., Dong H. and Halliday A. N. (1997) Dating of alteration episodes related to mercury mineralisation in the Almade´n district, Spain. *Earth Planet. Sci. Lett.* **148**, 287–298.

Hejing, W., Rahn, M., Xiaofeng, T., Nan, Z., Tingjing, X. (2008). Diagenesis and metamorphism of Triassic Fflysch along profile Zoige-Lushan, Northwest Sichuan, China. *Acta Geologica Sinica*. **82**, 917-926.

Hess, J.C and Lippolt, H.J. (1994). Compilation of K-Ar measurements on HD-B1 standard biotite. in : Odin G.S. (1994) : Phanerozoic time scale, Bull. Lias. Inform., IUGS subcom. Geochronol., 12, Paris p. 19-23.

Hetzel, R., Zwingmann, H., Mulch, A., Gessner, K., Akal, C., Hampel, A., Güngör, T., Petschick, R., Mikes, T. and Wedin, F. (2013) Spatiotemporal evolution of brittle normal faulting and fluid infiltration in detachment fault systems: a case study from the Menderes Massif, western Turkey. Tectonics 32, 1–13.

Hoffman, J. and Hower, J. (1979) Clay mineral assemblages as low grade metamorphic geothermometers: Application to the thrust faulted disturbed belt of Montana. In: Scholle, P.A. and Schluger, P.S., editors. Aspects of Diagenesis, SEPM Spec. Publ., 26, 55-79.

Işik V. and Uysal I.T., Caglayan A. and Seyitoglu G. (2014) The evolution of intra-plate fault systems in central Turkey: structural evidence and Ar–Ar and Rb–Sr age constraints for the Savcili Fault Zone. *Tectonics* **33**, 1875–1899.

Ji J. and Browne P.R.L. (2000) Relationship between illite crystallinity and temperature in active geothermal systems of New Zealand: Clay. Clay Miner. **48**, 139–144.

Kelley S. (2002) Excess argon in K–Ar and Ar–Ar geochronology. *Chem. Geol.* **188**, 1 – 22

Kirkland, C.L., Smithies, R.H., Woodhouse, A.J., Howard, H.M., Wingate, M.T.D., Belousova, E.A., Cliff, J.B., Murphy, R.C., Spaggiari, C.V. (2013). Constraints and deception in the isotopic record; the crustal evolution of the west Musgrave Province, central Australia. *Gondwana Research*, **23**, 759–781.

Korsch R.J., Lindsay, J.F. (1989). Relationships between deformation and basin evolution in the intracratonic Amadeus Basin, central Australia. *Tectonophysics*, **158**, 5-22.

Korsch R.J., Struckmeyer H.I.M. Kirkby L.J., Hutton L.J., Carr L.K., Hoffmann K., Chopping R., Roy I.G., Fitzell M., Totterdell J.M., Nicoll M.G. andTalabi B. (2011) Energy potential of the Millungera Basin: a newly discovered basin in north Queensland. *The APPEA Journal* **51**, 295-332.

Korsch R. J., Huston D. L., Henderson R. A., Blewett R. S., Withnall I. W., Fergusson C. L., Collins W. J., Saygin E., Kositcin N., Meixner A. J., Chopping R., Henson P. A., Champion D. C., Hutton L. J., Wormald R., Holzschuh J. and Costelloe R. D. (2012) Crustal architecture and geodynamics of North Queensland, Australia: insights from deep seismic reflection profiling. *Tectonophysics* **572-573**, 76-99.

Laurich B., Urai J.L., Desbois G., Vollmer C. and Nussbaum C. (2014). Microstructural evolution of an incipient fault zone in Opalinus Clay: Insights from an optical and electron microscopic study of ion-beam polished samples from the Main Fault in the Mt-Terri Underground Research Laboratory. *J. Struct. Geol*. **67**, 107-128.

Lee J. I. and Lee Y. I. (2001). Kübler illite crystallinity index of the Cretaceous Gyeongsang Basin, Korea: southeastern Korea: Implications for basin evolution. *Clays and Clay Minerals* **49**, 36–43.

Li H.-C., Ku T.-L., You C.-F., Cheng H., Lawrance Edwards R., Ma Z.-B., Tsai A.-S. and Li M.-D. (2005) 87Sr/86Sr and Sr/Ca in speleothems for paleoclimate reconstruction in Central China between 70 and 280 kyr ago. Geochim. Cosmochim. Acta 69, 3933–3947.

Li, Z. X., X. H. Li, P. D. Kinny, and J. Wang (1999), The breakup of Rodinia: Did it start with a mantle plume beneath south China? *Earth Planet. Sci. Lett*., **173**, 171–181

Li Z. X.; Bogdanova S. V., Collins A. S., Davidson A., De Waele B., Ernst R. E., Fitzsimons I. C. W., Fuck R. A., Gladkochub D. P., Jacobs J., Karlstrom K. E., Lul S., Natapov L. M., Pease V., Pisarevsky S. A., Thrane K., Vernikovsky V. (2008) Assembly, configuration, and break-up history of Rodinia: A synthesis. *Precambr. Res*. **160**,179–210.

Lin A. (1999) S–C cataclasite in granitic rock. *Tectonophysics* **304**, 257-273.

Lonker S.W. and Gerald J.D.F. (1990) Formation of coexisting 1M and $2M_1$ polytypes in illite from an active hydrothermal system. *Amer. Miner*. **75**, 1282-1289.

Ludwig K.R. (2012) User'sManual for Isoplot/Ex: a Geochronological Toolkit for Mi-crosoft Excel, 70pp.

Lupi, M., S. Geiger, and C. M. Graham (2010), Hydrothermal fluid flow within a tectonically active rift-ridge transform junction: Tjörnes Fracture Zone, Iceland, *J. Geophys. Res.*, **115**, B05104, doi:10.1029/2009JB006640.

Maffucci, R. Corrado, S., Aldega, L., Bigi, S., Chiodi, A., Di Paolo, L., Giordano, G. and Invernizzi, C. (2016). Cap rock efficiency of geothermal systems in fold-and-thrust belts: Evidence from paleo-thermal and structural analyses in Rosario de La Frontera geothermal area (NW Argentina). *Journal of Volcanology and Geothermal Research*, **328**, 84-95.

Mancktelow N., Zwingmann H., Campani M., Fugenschuh B., Mulch A. (2015) Timing and conditions of brittle faulting on the Silltal-Brenner Fault Zone, Eastern Alps (Austria). *Swiss J Geosci* **108**, 305–326.Mancktelow, N., Zwingmann, H. and Mulch, A. (2016) Dating of fault gouge from the Naxos detachment (Cyclades, Greece). Tectonics 35 (10), 2334–2344.

McDougall, I., Roksandic, Z. (1974). Total fusion 40Ar/39Ar ages using HIFAR reactor. Journal of the Geological Society of Australia, 21, 81-89.

Merrriman R. J. and Frey M. (1999) Patterns of very low-grade metamorphism in metapelitic rocks. In *Low Grade Metamorphism* (eds. M. Frey and D. Robinson). Blackwell Science, Cambridge. pp. 61–107.

Merrriman R. J. and Peacor D.R. (1999) Very low-grade metapelites: mineralogy, microfabrics and measuring reaction progress. In *Low Grade Metamorphism* (eds. M. Frey and D. Robinson). Blackwell Science, Cambridge. pp. 10–60.

Michalski, J.R., Reynolds, S.J., Niles, P.B., Sharp, T.G. and Christensen, P.R. (2007). Alteration mineralogy in detachment zones: Insights from Swansea, Arizona. Geosphere, 3, 84–198.

Middleton A.W., Uysal I.T., Bryan S.E., Hall C.M. and Golding S.D (2014) Integrating ^{40}Ar–^{39}Ar, ^{87}Rb–^{87}Sr and ^{147}Sm–^{143}Nd geochronology of authigenic illite to evaluate tectonic reactivation in an intraplate setting, central Australia. *Geochim. Cosmochim. Acta.* **134**, 155-174.

Mutlu H., Uysal I. T., Altunel, E., Karabacak V., Feng Y., Zhao J.-x. and Atalay O. (2010) Rb–Sr systematics of fault gouges from the North Anatolian Fault Zone (Turkey), J. Struct. Geol. **32**, 216-221.

Myers, J.S., Shaw, R.D. and Tyler, I.M. (1996). Tectonic evolution of Proterozoic Australia, *Tectonics*, **15**, 1431–1446.

Neumann, N.L. and Kositcin, N. (2011). New SHRIMP U-Pb zircon ages from north Queensland, 2007–2010. *Geoscience Australia, Record*, **2011/38**, 82 p.

Nicchio M.A., Nogueira F.C., Balsamo F., Souza J.A., Carvalho B.R. and Bezerra F.H. (2018) Development of cataclastic foliation in deformation bands in feldspar-rich conglomerates of the Rio do Peixe Basin, NE Brazil. *J. Struct. Geol*. **107**, 132-141.

O'Dea, M. G., Lister, G. S., MacCready, T., Betts, P. G., Oliver, N. H. S., Pound, K. S., Huang, W. and Valenta, R. K. 1997. Geodynamic evolution of the Proterozoic Mount Isa terrain. In Orogeny Through Time, Edited by: Burg, J. P. and Ford, M. Vol. 121, 99–122. Geological Society of London Special Publication.

Odin G.S. and 35 collaborators (1982). Interlaboratory standards for dating purposes. in: Odin, G.S. (editor) Numerical Dating in Stratigraphy. Part 1. John Wiley & Sons, Chichester, 123-148.

Ohr M., Halliday A.N. and Peacor D.R. (1994) Mobility and fractionation of rare earth elements in argillaceous sediments: Implications for dating diagenesis and low-grade metamorphism. *Geochim. Cosmochim. Acta.* **58**, 289-312.

Parry, W. T., Hedderly-Smith, D., And Bruhn, R. L. (1991), Fluid Inclusions and Hydrothermal Alteration on the Dixie Valley Fault, Nevada. *J. Geophys. Res*., **96**, 19,733-19,748.

Rosenbaum G., Uysal I.T. and Babaahmadi A. (2015) The Red Rock Fault Zone (northeast New South Wales): Kinematics, timing of deformation and relationships to the New England oroclines. Aust. J. Earth. Sci. **62**, 409-423.

Rossetti, F., Aldega, L., Tecce, F., Balsamo, F. (2011) Fluid flow within the damage zone of the Boccheggiano extensional fault (Larderello–Travale geothermal field, central Italy): structures, alteration and implications for hydrothermal mineralization in extensional settings. *Geological Magazine* **148**, 558–579.

Rowe C.D., Kirkpatrick J.D. and Brodsky E.E. (2012) Fault rock injections record paleo-earthquakes. *Earth Planet. Sci. Lett*. **335**, 154-166.

Rutter E.H., Maddock R.H., Hall S.H. and White S.H. (1986) Comparative microstructures of natural and experimentally produced clay-bearing fault gouges. Pure Appl. Geophys. **124**, 3-30.

Schmid S. M. and M. R. Handy (1991) Towards a genetic classification of fault rocks: Geological usage and tectonophysical implications. In Controversies in Modern Geology: Evolution of Geological Theories in Sedimentology, Earth History and Tectonics (eds. D. W. Mueller, J. A. McKenzie and H. Weissert). Academic, San Diego, Calif. pp. 339–361.

Schmidt P.W., Williams G.E., Camacho A. and Lee, J.K.W. (2006) Assembly of Proterozoic Australia: implications of a revised pole for the ∼1070 Ma Alcurra Dyke Swarm, central Australia. *Geophys. J. Int*. **167**, 626–634.

Schneider, J., Haack, U., Stedingk, K. (2003). Rb-Sr dating of epithermal vein mineralization stages in the eastern Harz Mountains (Germany) by paleomixing lines. *Geochimica et Cosmochimica Acta*, **67**, 1803-1819.

Scott, D.L., Rawlings, D.J., Page, R.W., Tarlowski, C.Z., Idnurm, M., Jackson, M.J. and Southgate, P.N., (2000) Basement framework and geodynamic evolution of the Palaeoproterzoic superbasins of north- central Australia: an integrated review of geochemical, geochronological and geophysical data. Australian Journal of Earth Sciences, 47, 341-380.

Sharp Z. D. (1990) A laser-based microanalytical method for the in situ determination of oxygen isotope ratios of silicates and oxides: *Geochim. Cosmochim. Acta.* **54**, 1353-1357.

Sibson R. H. (1977) Fault rocks and fault mechanisms. *J. Geol. Soc. Lond.* **133**, 191–213.

Sibson R. H. (1987) Earthquake rupturing as a hydrothermal mineralising agent. *Geology* **15**, 701-704.

Sibson R.H. (1989) Earthquake faulting as a structural process. Journal of Structural *Geology* **11**, 1-14.

Smeraglia, L., Aldega, L. Billi, A., Carminati, E., Doglioni, C. (2016). Phyllosilicate injection along extensional carbonate-hosted faults and implications for co-seismic slip propagation: case studies from the central Apennines, Italy. *J. Struct. Geol*., **93**, 29-50.

Solum J.G. van der Pluijm, B.A. and Peacor D.R. (2005) Neocrystallization, fabrics and age of clay minerals from an exposure of the Moab Fault, Utah. J. Struct. Geol. **27**, 1563-1576.

Srodon J. and Eberl, D.D. 1984. Illite. In *Micas*. (ed. S.W. Bailey). Reviews in mineralogy 13, Mineralogical Society of America. pp. 495-544.

Steiger R.H. and Jäger E. (1977) Subcommission on geochronology: convention on the use of decay constants in geochronology and cosmochronology. *Earth. Planet. Sci. Lett*. **36**, 359–362.

Tanaka H. and Idnurm. M (1994). Palaeomagnetism of Proterozoic mafic intrusions and host rocks of the Mount Isa Inlier, Australia: revisited. *Precambr. Res*. **69**, 241-258.

Taylor S.R. and McLennan S.M. (1985) *The Continental Crust: Its Composition and Evolution*. Blackwell, 312.

Taylor H. P. (1997) Oxygen and hydrogen isotope relationships in hydrothermal mineral deposits. In *Geochemistry of hydrothermal ore deposits.* (ed. H. L. Barnes). John Wiley, New York. pp. 229–288.

Torgersen E., Viola G., Zwingmann H. and Harris C. (2014) Structural and temporal evolution of a reactivated brittle-ductile fault—Part II: timing of fault initiation and reactivation by K-Ar dating of synkinematic illite/muscovite. *Earth. Planet. Sci. Lett.* **407**, 221–233

Ujiie K., Yamaguchi A., Kimura G. and Toh, S. (2007) Fluidization of granular material in a subduction thrust at seismogenic depths. *Earth. Planet. Sci. Lett.*, **259**, 307-318.

Uysal I.T. and Golding S.D. (2003) Rare earth element fractionation in authigenic illite-smectite from Late Permian clastic rocks, Bowen Basin, Australia: implications for physico-chemical environments of fluids during illitization. *Chem. Geol*. **193**, 167-179.

Uysal I.T., Glikson M., Golding S.D. and Southgate P.N. (2004) Hydrothermal control on organic matter alteration and illite precipitation, Mt Isa Basin, Australia. *Geofluids* **4**, 131-142.

Uysal I.T., Mory A.Y., Golding S.D., Bolhar R. and Collerson K.D. (2005). Clay mineralogical, geochemical and isotopic tracing of the evolution of the Woodleigh impact structure, Southern Carnarvon Basin, Western Australia. Contrib. Mineral. Petrol. **149**, 576-590.

Uysal I. T., Mutlu M, Altunel A., Karabacak V. and Golding S. D. (2006) Clay mineralogical and isotopic (K–Ar, δO-18, δD) constraints on the evolution of the North Anatolian fault zone, Turkey. *Earth. Planet. Sci. Lett.* **243**, 181–194.

Uysal I.T., Golding S.D, Bolhar R., Zhao J-X., Feng Y., Greig A. and Baublys K. (2011) CO_2 degassing and trapping during hydrothermal cycles related to Gondwana rifting in eastern Australia. *Geochim. Cosmochim. Acta.* **75**, 5444–5466.

Vance D, Ayres M, Kelley SP and Harris NBW (1998) The thermal response of a metamorphic belt to extension: constraints from laser Ar data on metamorphic micas. *Earth. Planet. Sci. Lett.* **162**,153-164

van der Pluijm B.A., Hall C.M., Vrolijk P.J., Pevear D.R. and Covey M.C. (2001) The dating of shallow faults in the Earth's crust. *Nature* **412**: 172-175.

Verdel C., van der Pluijm,B. A. and Niemi N. (2012) Variation of illite/muscovite 40Ar/39Ar spectra during progressive low-grade metamorphism: an example from the US Cordillera. *Contrib. Mineral. Petr*. **164**, 521–536.

Villa, I.M. De Bièvre, P.; Holden, N.E.; Renne, P.R. (2015). IUPAC-IUGS recommendation on the half life of 87Rb. Geochimica et cosmochimica acta, 164, 382-385.

Viola G, Zwingmann, H., Mattila, J., Käpyaho, 2013. K-Ar illite age constraints on the Proterozoic formation and reactivation history of a brittle fault in Fennoscandia. Terra Nova. **25**, 236-244.

Viola G., Scheiber T., Fredin O., Zwingmann H., Margreth A., Knies J. (2016) Deconvoluting complex structural histories archived in brittle fault zones. Nat. Commun. **7**, 13448, 1-10.

Vrolijk P. and van der Pluijm B.A. (1999) Clay gouge. *J. Struct. Geol*. **21**, 1039-1048.

Walker, J.R. and Thompson, G.R. (1990). Structural variations in chlorite and illite in a diagenetic sequence from the Imperial Valley, Caslifornia. *Clays and Clay Minerals*. **38**, 315-321.

Walter, M.R., Veever, J.J., Calver, C.R., Grey, K. (1995). Neoproterozoic stratigraphy oft he Centralian Superbasin, Australia. *Precambrian Research*, **73**, 173-195.

Warr L.N. and Nieto, F. (1998) Interlaboratory standardization and calibration of clay mineral crystallinity and crystallite size data. J. Metamorph. Geol. **12**, 141–152

Warr L. N. and Mählmann R.F. (2015) Recommendations for Kübler Index standardization. *Clay Miner*. **50**, 283–286.

Wendt, I. (1993). Isochron or mixing line? *Chemical geology*, **104**, 301-305.

Withnall, IW., Hutton, LJ., Armit, RJ., Betts, PG., Blewett, RS., Champion, DC., and Jell, PA. (2013). North Australian Craton. In P. A. Jell (Ed.), Geology of Queensland (pp. 23-112). Brisbane Qld Australia: Geological Survey of Queensland.

Yamasaki S., Zwingmann H., Yamada K., Tagami T. & Umeda K. (2013) Constraining timing of brittle deformation and faulting in the Toki granite, central Japan. Chemical Geology, 351, 168–174.

Zwingmann, H. and Mancktelow, N. (2004) Timing of Alpine fault gouges. Earth Planet. Sci. Lett. 223 (2–4), 415–425.

Zwingmann H., Mancktelow N., Antognini M., Lucchini R. (2010) Dating of shallow faults—new constraints from the Alp Transit tunnel site (Switzerland). *Geology* **38**, 487–490.

Figure captions

Figure 1. (a) Simplified map of north-central Australia showing the interpreted subsurface distribution of the Millungera Basin. The surface distribution of Cenozoic and Mesozoic sediments and the locations of the Proterozoic–Ordovician Basins are also shown (modified from Korsch et al., 2011). (b) Interpreted migrated seismic section for part of seismic line 07GA-IG1 across the Millungera Basin, showing interpreted structures and sequence boundaries below the base Carpentaria unconformity (from Korsch et al., 2011).

Figure 2. Photos of sampled cores showing fault gouges investigated in this study. Foliated and veined clay-rich fault gouges with light grey – green colour distinctive from adjacent brown hematite-rich sandstone host rock (a-e). Fault gouge veins are characterized by an ultrafine-to fine-grained matrix and angular to sub-angular fragments of host sandstone of various sizes, ranging from submicron to centimetres (b). Ultracataclastic veins are common, which are observed as simple veins, complex lenses, and networks (c-d). Foliated fault gouge zone with alternating red hematite-rich and grey – green layers (e). Slickenside structure is a commonly seen at the sharp contact between the clay-rich fault gouge layers and the host rock (f-g).

Figure 3. Thin section photomicrographs (a-b) and SEM images (c-f) illustrating fault gouge illites from the Millungera Basis. (a) Illite plates (white) occur in voids within detrital quartz grains and as pore-filling clay together with chlorite between detrital grains. Note green – yellow chlorite shown by red arrow. (b) Alteration of detrital muscovite in illite. Note illite plates at the ends of the mica filling pores. (c) SEM image of sample Dob-441. Note the large detrital mica grain (>2 μm) with diffuse-blurred and irregular edges (the white material on the right-hand site), while authigenic illites occur in smaller crystals (<2 μm) with straight edges. SEM image of upper anchi-and epizone sample Dob-476.6. Note rounded smaller

crystals (arrows), which occur partly as a constituent of larger illite plates (dashed arrows). (e-f) SEM images of samples JC-408 and JC-360.7, respectively. Note euhedral (hexagonal) and anhedral crystal plates with sharp and straight edges of these JC samples, which occur in smaller crystal size in comparison to the Dob samples. Smaller crystal size is consistent with higher KI values of JC samples (see Table 1).

Figure 4. Microstructures of a faulted sample from Julia Creek 1 well (depth 360 m), petrographic thin section is cut parallel to the inferred shear direction. A) Whole thin section image collected using an optical microscope in plane polarised light showing composite S-C foliation (red dashed lines illustrate the orientation of the S plane. B) Optical microscope image in cross polarised light showing phyllosilicate enriched C-planes and the oblique S-foliation. C) Optical microscope image in cross polarised light showing alignment of opaque insoluble minerals along the S-plane (highlighted by the red arrows) indicative of pressure solution. D and E) Scanning electron microscope images of the deformed rock showing corroded boundaries in detrital quartz (Qtz) highlighted by the red arrows, authigenic kaolinite and illite (Kln; Ill) and detrital muscovite (Ms) aligned along the C plane.

Figure 5: Faulted sample from Dobbyn 2 well (depth 441 m). A) Hand specimen showing green-beige slickenside surface with striations due to frictional movement along the surface. B) Polished face of the hand specimen cut parallel to the shear direction as inferred from the striation direction shown in A). C) Whole thin section image collected using an optical microscope in planes polarised light. The position of the thin section with respect to the hand specimen is shown by the red rectangle in B); yellow dashed line bound different microstructural domains of the fault rock defined as i) foliated cataclasite and ii) cataclasite. White boxes indicate the location of the following images. D) Optical microscope image in plane polarised light showing the slickenside surface (bound by the yellow dashed line) of the samples being composed of iso-aligned phyllosilicates. Also shown is a hematite rich

injection vein. E) Scanning electron microscope image of the foliated cataclasite portion of the samples and the characteristic S-C-C' texture (see text for details). White dashed line highlights the orientation of the S-planes. F) Optical microscope image in plane polarised light showing a slip surface (bound by the yellow dashed line) at the boundary between the foliated and non-foliated cataclasite domains. G) Optical microscope image in plane polarised light showing a network of hematite filled intra-crystalline micro-fractures in the cataclasite domain of the fault rock, mainly composed of quartz (white grains) and pore filling clays.

Figure 6. Ar–Ar dating results and argon release diagrams for illites from the fault gouges of <2 μm size fraction, for sanple Dob-476.6 (a), Dob-441 (b), JC-408, and JC-360.7 (c). Note consistent Ar–Ar total gas ages except for sample Dob-476.6.

Figure 7. A) Histogram for K–Ar and Ar–Ar ages and probability distribution of ages for fault gouge illites. Curves show relative probabilities calculated using Isoplot 7 for Excel (Ludwig, 2012). B) K–Ar and Ar–Ar dates (no error bars due to small errors) for different size fractions of fault gouges and C) matrix illites from host rocks and their interpretation in relation to tectonic history.

Figure 8. A) Rb-Sr data of the different size fractions and the untreated, leachate and residue separates of each size fractions from sample. Parallel linear relationships correspond to similar isochron age, but with different initial $^{87}Sr/^{86}Sr$ values. B) Rb-Sr plot for untreated and residues of <2 μm fractions from most Julia Creek 1 samples. C)Well-defined isochron for Julia Creek 1 samples after omitting two untreated aliquots D) Rb–Sr isochron diagrams for an assemblage of Dobbyn 2 samples (including JC-360.7B <0.5 μm) and E) another group of Dobbyn 2 samples with a younger age.

Figure 9. REE patterns of the fault gouge illites. Note that the illites are substantially enriched in light REE (LREE) relative to PAAS.

Figure 10. KI values versus present depth from boreholes Jolokia 1 and Dobbyn 2.

Figure 11. Correlations between K–Ar ages and KI values for fault gouge illites for samples from Dobbyn 2 (A), Julia Creek 1 (B) and matrix illites from sandstone host rocks (C) (>2µm fractions were not included). Analytical errors of K–Ar ages were disregarded for the regression lines. Exponential trends were obtained for the best fit of the regression lines for Dobbyn 2 samples (A). Note the flat trends that are obvious for Julia Creek 1 samples for fault gouges (B) and matrix illites (C).

Figure 12. Summary of the geological history of the Millungera basin region and isotopic age clusters of the illites.

Table 1. Clay mineralogy and age data of fault gouges and host rocks from Julia Creek 1 (JC) and Dobbyn 2 (Dob).

Sample & size fraction	Clay mineralogy	KI ($\Delta 2\theta$)	AI ($\Delta 2\theta$)	Very-low-grade metamorphic zone	$2M_1$ %	1M %	$1M_d$ %	Rb–Sr isochron age (Ma) (2σ)	Ar–Ar total gas age (Ma) (1σ)	K–Ar age (Ma) (2σ)	K_2O (%)	$^{40}Ar_{rad}$ (%)	$^{40}Ar_{rad}$ (10^{-10}mol/g)
Fault gouge													
JC-321 <2mm	illite	0.59		Diagenesis									
JC-326.1 <2μm	illite	0.69		Diagenesis									
JC-343.3 <2μm	illite, kaol., chl.	0.63		Diagenesis	68	14	18			1044.0 ± 24.4	7.10	99.3	174.1
JC-343.3 0.5-0.1μm	illite, kaol., chl.	0.79		Diagenesis						1039.2 ± 24.0	6.86	99.7	167.2
JC-343.3 <0.1μm	illite	0.92		Diagenesis						1025.3 ± 23.7	6.33	99.6	151.6
JC-360.7 <2μm	illite, kaol., chl.	0.63		Diagenesis	66	18	16	1023 ± 12	1038.1 ± 2.9	1014.9 ± 23.7	7.61	99.3	179.8
JC-360.7 2-1μm	illite, kaol., chl.	0.65		Diagenesis	58	22	20			1038.9 ± 24.0	7.49	99.4	182.5
JC-360.7 <1μm	illite, kaol., chl.	0.73		Diagenesis						1041.1 ± 24.1	7.49	99.5	183.0
JC-360.7 <0.5μm	illite	0.75		Diagenesis				1033 ± 25		1005.5 ± 23.1	7.65	99.6	178.6
JC-387.8 <2μm	illite, kaol., chl.	0.57		Diagenesis				1023 ± 12					
JC-408 >2μm	illite, kaol., chl.	0.42		Upper anchizone						1243.2 ± 29.1	7.64	99.7	237.1
JC-408 2-1μm	illite, kaol., chl.	0.63		Diagenesis	63	14	23			1118.7 ± 25.9	7.94	99.6	213.4
JC-408 <2μm	illite, kaol., chl.	0.60		Diagenesis	64	17	19		1040.0 ± 2.3	1115.8 ± 26.1	7.88	99.5	211.1
JC-408 <1μm	illite, kaol., chl.	0.70		Diagenesis	64	15	22			1118.2 ± 25.9	7.81	96.6	209.8
JC-408 <0.5μm	illite	0.82		Diagenesis						1104.0 ± 25.4	7.82	99.7	206.5
JC-430.4 <2μm	illite, kaol., chl.	0.51		Lower anchizone									
JC-440.5 <2μm	illite, kaol., chl.	0.44		Lower anchizone	58	24	18	1023 ± 12		1048.9 ± 24.5	6.60	99.4	176.3
JC-440.5 0.5-0.1μm	illite, kaol., chl.	0.84		Diagenesis						1020.3 ± 23 .6	7.41	99.8	168.8
JC-440.5 <0.1μm	illite	1.01		Diagenesis						1017.6 ± 23 .5	7.12	99.8	168.8
JC-473-A <2μm	illite, chl.	0.51	0.35	Lower anchizone									
JC-473-B <2μm	illite, chl.	0.47		Lower anchizone									
JC-483.2 <2μm	illite, chl.	0.60	0.42	Diagenesis									
Dob-389.6 2-1μm	illite, kaol., chl.	0.42		Upper anchizone	95		5	1000±12		1081.8 ± 25.0	5.97	99.7	153.5
Dob-389.6 <2μm	illite, kaol., chl.	0.43		Upper anchizone	90		10	1033 ± 25		1071.2 ± 25.0	6.53	99.7	165.7
Dob-389.6 1-0.5μm	illite, kaol., chl.	0.51		Lower anchizone	90		10			1037.8 ± 24.0	7.32	99.6	178.1
Dob-389.6 0.5-0.1μm	illite, kaol.	0.62		Diagenesis	80		20	1000±12		1053.0 ± 24.3	7.20	99.7	178.6
Dob-389.6 <0.5μm	illite, kaol.	0.63		Diagenesis						981.8 ± 22.6	7.63	99.8	172.7
Dob-389.6 <0.1μm	illite, kaol.	1.00		Diagenesis						905.4 ± 20.9	6.62	99.6	135.0
Dob-417 <2μm	illite, kaol., chl.	0.50		Lower anchizone									
Dob-441 >2μm	illite, kaol., chl.	0.36		Upper anchizone						1312.3 ± 30.7	3.72	99.5	124.5
Dob-441 <2μm	illite, kaol., chl.	0.42		Upper anchizone	95		5	1033 ± 25	1068.1 ± 1.8	1148.7 ± 26.9	4.98	99.3	138.7

Dob-441 <1µm	illite, kaol., chl.	0.51		Lower anchizone	95	5			1086.5 ± 25.1	6.10	99.4	157.7
Dob-441 <0.5µm	illite, kaol., chl.	0.42		Upper anchizone					1063.3 ± 24.4	6.05		
Dob-449.1 <2µm	illite, kaol., chl.	0.29		Epizone	100		1033 ± 25		949.1 ± 22.2	6.40	99.5	138.6
Dob-449.1 2-0.5µm	illite, kaol., chl.	0.39		Upper anchizone			1000±12		924.9 ± 21.4	6.63	99.8	138.9
Dob-449.1 1-0.5µm	illite, kaol., chl.	0.35		Upper anchizone					903.1 ± 20.9	6.73	99.6	136.8
Dob-449.1 <0.5µm	illite, kaol., chl.	0.37		Upper anchizone					912.6 ± 21.1	5.43	100	111.9
Dob-449.3 >2µm	kaol., illite, chl.	0.14		Epizone					1259.0 ± 29.1	0.402	100	12.70
Dob-449.3 <2µm	illite, kaol., chl.	0.19		Epizone								
Dob-449.3 2-1µm	kaol., chl., illite	0.21		Epizone					1047.7 ± 24.2	0.294	100	7.24
Dob-449.3 1-0.5µm	kaol., chl., illite	0.27		Epizone					1117.2 ± 25.8	0.554	99.4	14.87
Dob-449.3 0.5-0.2µm	kaol., chl., illite	0.25		Epizone					950.9 ± 22.0	6.02	99.7	130.7
Dob-449.3 <0.5µm	kaol., chl., illite	0.25		Epizone					1004.4 ± 23.2	0.428	99.8	9.98
Dob-476.6 >2µm	illite, kaol., chl.	0.26		Epizone					1170.4 ± 27.4	2.15	99.5	61.43
Dob-476.6 2-1µm	illite, kaol., chl.	0.29		Epizone	100				975.7 ± 22.2	4.43	99.4	101.7
Dob-476.6 <2µm	illite, kaol., chl.	0.33		Upper anchizone	100		1000 ± 12	994.6 ± 2.2	983.7 ± 23.0	4.80	99.4	108.9
Dob-476.6 <1µm	illite, kaol., chl.	0.31		Epizone	100				922.2 ± 21.2	6.18	100.0	129.0
Host whole rock												
JC-360.6 <2µm	illite	0.48		Lower anchizone								
JC-360.6 2-1µm	illite	0.68		Diagenetic					1066.9 ± 24.6	6.13	99.61	157.7
JC-360.6 1-0.5µm	illite	0.82		Diagenetic					1065.4 ± 24.6	6.90	99.7	173.8
JC-360.6 0.5-0.2µm	illite	0.52		Lower anchizone					1053.8 ± 24.3	6.68	99.2	165.8
JC-360.6 <0.2µm	illite	0.78		Diagenesis					928.3 ± 47.6	6.63	99.05	139.6
JC-490.2 <2µm	illite, chl.	0.46	0.36	Lower anchizone								
JC-500 <2µm	illite, chl.	0.51	0.36	Lower anchizone								
JC-500 2-1µm	illite, chl.	0.66		Diagenesis					1092.0 ± 25.2	3.37	99.69	87.71
JC-500 1-0.5µm	illite, chl.	0.62		Diagenesis					1076.8 ± 24.8	5.15	99.67	131.6
JC-500 0.5-0.2µm	illite, chl.	0.64		Diagenesis					1066.7 ± 24.5	5.39	99.47	135
JC-500 <0.2µm	illite, chl.	0.63		Diagenesis					878.3 ± 45.1	5.41	99.02	106.2
Dob-499.4 >2µm	illite, kaol., chl.	0.22		Epizone					1156.2 ± 26.6	0.37	97.1	10.26
Dob-499.4 <2µm	illite, kaol., chl.	0.20		Epizone								
Dob-499.4 2-1µm	illite, kaol., chl.	0.23		Epizone					1115.8 ± 25.7	2.03	99.6	54.38
Dob-499.4 1-0.5µm	illite, kaol., chl.	0.20		Epizone					1047.3 ± 24.1	5.08	99.5	125.1
Dob-499.4 0.5-0.2µm	illite, kaol., chl.	0.18		Epizone					1068.2 ± 24.6	3.30	99.3	83.41
Dob-499.4 <0.2µm	illite, kaol., chl.	0.21		Epizone					1025.6 ± 52.6	3.63	97.5	86.97

Calibration of the illite crystallinity (IC) and chlorite crystallinity (ChC) values and determination of very-lowe-grade- metamorthic zones. has been done according to Warr and Mählmann (2015) and Warr and Cox (2016). kaol. = kaolinite, chl. = chlorite. Illite polytype percentages are relative to total illite

Table 2. K-Ar standard and airshot data.

STANDARD ID	K [%]	Rad. ^{40}Ar (mol/g)	Rad. ^{40}Ar (%)	Age (Ma)	Error (Ma)	% difference from re-commended reference age
HD-B1-137	7.96	3.3431E-10	89.76	24.1	0.4	-0.01
LP6-151	8.37	1.9477E-09	97.28	129.4	1.8	1.19
HD-B1-139	7.96	3.4214E-10	92.33	24.6	0.3	1.73
LP6-153	8.37	1.9465E-09	97.32	129.3	1.7	1.12
HD-B1-140	7.96	3.3805E-10	92.39	24.3	0.3	0.50
LP6-154	8.37	1.9196E-09	97.39	127.6	1.6	-0.23
HD-B1-141	7.96	3.4399E-10	92.86	24.8	0.3	2.27
LP6-155	8.37	1.9304E-09	97.69	128.3	1.6	0.31
HD-B1-142	7.96	3.4500E-10	93.28	24.8	0.3	2.56
LP6-156	8.37	1.9285E-09	97.59	128.2	1.7	0.21
HD-B1-147	7.96	3.4124E-10	92.88	24.6	0.3	1.45
LP6-161	8.37	1.9257E-09	97.13	128.0	1.7	0.07
HD-B1-148	7.96	3.3633E-10	90.67	24.2	0.3	0.00
LP6-162	8.37	1.9236E-09	97.21	127.9	1.7	-0.03
HD-B1-149	7.96	3.3562E-10	90.93	24.2	0.3	-0.21
LP6-163	8.37	1.9234E-09	97.21	127.9	1.6	-0.04

Airshot ID	$^{40}Ar/^{36}Ar$	+/-
AS131-AirS-1	295.67	0.45
AS131-AirS-2	293.43	0.46
AS133-AirS-1	298.42	0.14
AS133-AirS-2	297.35	0.29
AS134-AirS-1	295.81	0.14
AS134-AirS-2	296.65	0.08
AS135-AirS-1	296.59	0.13
AS135-AirS-2	296.76	0.17
AS136-AirS-1	295.22	0.24
AS136-AirS-2	296.69	0.27
AS141-AirS-1	295.85	0.28
AS141-AirS-2	296.53	0.23
AS142-AirS-1	294.87	0.23
AS142-AirS-2	296.52	0.18
AS143-AirS-1	294.16	0.20
AS143-AirS-2	296.81	0.17

HD-B1: Hess and Lippolt (1994).

LP-6: Odin et al. (1982).

Recommended $^{40}Ar/^{36}Ar$ value: 295.5: Steiger and. Jäger (1977).

The accepted age value of HD-B1 is 24.21 ± 0.32 Ma and 127.9 ± 1.5 Ma for LP6

Table 3. ^{87}Rb-^{86}Sr data for the untreated (U) and acid leached residues (R) of different clay fractions from the Milungera Basin fault gouges.

Sample	Size farction (μm)	Rb (ppm)	Sr (ppm)	$^{87}Rb/^{86}Sr$	$^{87}Sr/^{86}Sr$	±2σ
JC-343.3U	<2	263.8	244.7	3.14	0.771035	0.000008
JC-360.7U[b-c]	<2	270.5	303.9	2.59	0.757396	0.000009
JC-360.7R[b-c]	<2	253.7	269.0	2.74	0.759576	0.000009
JC-360.7R	2-1	279	361.1	2.25	0.754344	0.000008
JC-360.7L	2-1	61.96	914.2	0.196	0.715331	0.000006
JC-360.7R[d]	<0.5	288.7	222.1	3.79	0.778401	0.000005
JC-360.7L	<0.5	68.94	906.2	0.220	0.715632	0.000006
JC-387.8U[b]	<2	203.7	564.6	1.05	0.734125	0.000009
JC-387.8R[b-c]	<2	201.6	537.4	1.09	0.735621	0.000007
JC-408U	<2	273.0	259.4	3.06	0.768788	0.000009
JC-440.5U[b]	<2	206.8	637.0	0.941	0.733108	0.000007
JC-440.5R[b-c]	<2	213.2	627.4	0.986	0.734396	0.000009
JC-440.5R	<0.5	279.2	240.1	3.38	0.765505	0.000006
JC-440.5L	<0.5	26.75	378.4	0.205	0.716576	0.000006
Dob-389.6U[d]	2	239.5	184.5	3.78	0.778229	0.000009
Dob-389.6R[e]	2-1	255.0	254.5	2.92	0.769394	0.000006
Dob-389.6R[e]	<0.5	268.6	201.0	3.89	0.783259	0.000008
Dob-389.6L	<0.5	22.08	612.8	0.10	0.712000	0.000006
Dob-441U[d]	<2	134.8	121.6	3.23	0.770115	0.000008
Dob-441R	2-1	200.7	203.4	2.87	0.767702	0.000006
Dob-441R	<1	202.1	201.8	2.91	0.768636	0.000007
Dob-441L	<1	20.5	399.5	0.149	0.720827	0.000006
Dob-449.1U[d]	<2	214.7	337.0	1.85	0.750186	0.000009
Dob-449.1R[d]	<2	218.9	326.1	1.95	0.751971	0.000014
Dob-449.1R[d]	2-1	242.0	378.8	1.86	0.749952	0.000006
Dob-449.1L	2-1	13.59	265.7	0.148	0.718102	0.000006
Dob-476.6U[e]	<2	190.0	521.6	1.06	0.744176	0.000009
Dob-476.6R[e]	<2	200.2	517.7	1.12	0.744209	0.000007

U= untreated, R = residue, L = leachate

Samples with superscript b, c, d, and e are used in Fig. 8b, c, d, and e, respectively.

Table 4. Trace element data (ppm) for the fault gouge illites.

Sample	JC-360.7	JC-387.8	JC-440.5	Dob-389.6	Dob-449.1	Dob-476.6	PAAS
La	89.8	281.5	242.3		328.0	396.2	38.0
Ce	193.9	619.1	519.4		591.8	773.3	80.0
Pr	19.9	63.1	54.3		73.1	80.2	8.90
Nd	69.1	225.6	187.3		257.0	271.5	32.0
Sm	12.8	39.1	32.2		44.5	46.3	5.60
Eu	2.22	4.32	4.22		7.30	7.01	1.10
Gd	9.27	24.3	21.2		29.8	28.7	4.70
Tb	1.05	2.07	2.59		3.70	3.23	0.77
Dy	5.09	7.22	12.9		20.2	15.9	4.40
Ho	0.94	1.17	2.42		4.36	3.29	1.00
Er	2.59	3.27	6.66		14.2	10.5	2.90
Tm	0.37	0.43	0.97		2.47	1.74	0.40
Yb	2.36	2.81	6.29		18.0	12.3	2.80
Lu	0.35	0.41	0.93		2.87	1.93	0.43
Th	80.8	110.9	83.6		107.7	149.1	14.60
U	7.54	8.43	18.6		32.2	40.3	3.10
Sc	20.7	10.2	11.2		91.4	58.1	16.00
(La/Lu)$_c$	29	23	76		13	29	10
Th/Sc	3.9	10.9	7.5		1.2	2.6	0.9
Th/U	10.7	13.2	4.5		3.3	3.7	4.7

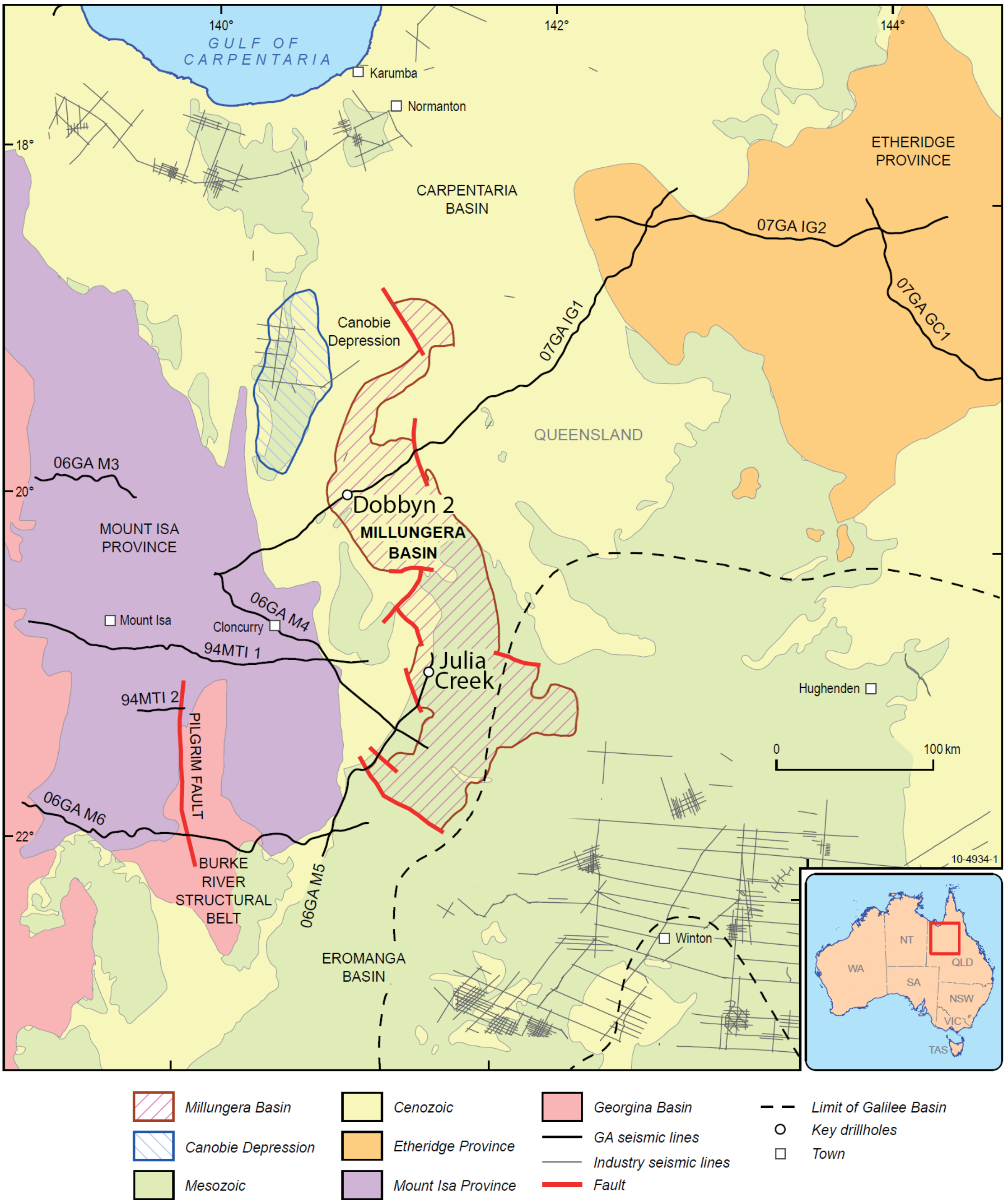
140°
142°
144°
18°
20°
22°
GULF OF CARPENTARIA
Karumba
Normanton
CARPENTARIA BASIN
ETHERIDGE PROVINCE
07GA IG2
07GA GC1
07GA IG1
Canobie Depression
QUEENSLAND
06GA M3
MOUNT ISA PROVINCE
Dobbyn 2
MILLUNGERA BASIN
06GA M4
Mount Isa
Cloncurry
94MTI 1
Julia Creek
Hughenden
94MTI 2
PILGRIM FAULT
0
100 km
06GA M6
BURKE RIVER STRUCTURAL BELT
06GA M5
EROMANGA BASIN
Winton
10-4934-1
NT
WA
SA
QLD
NSW
VIC
TAS
Millungera Basin
Canobie Depression
Mesozoic
Cenozoic
Etheridge Province
Mount Isa Province
Georgina Basin
GA seismic lines
Industry seismic lines
Fault
Limit of Galilee Basin
Key drillholes
Town

Figure 1a

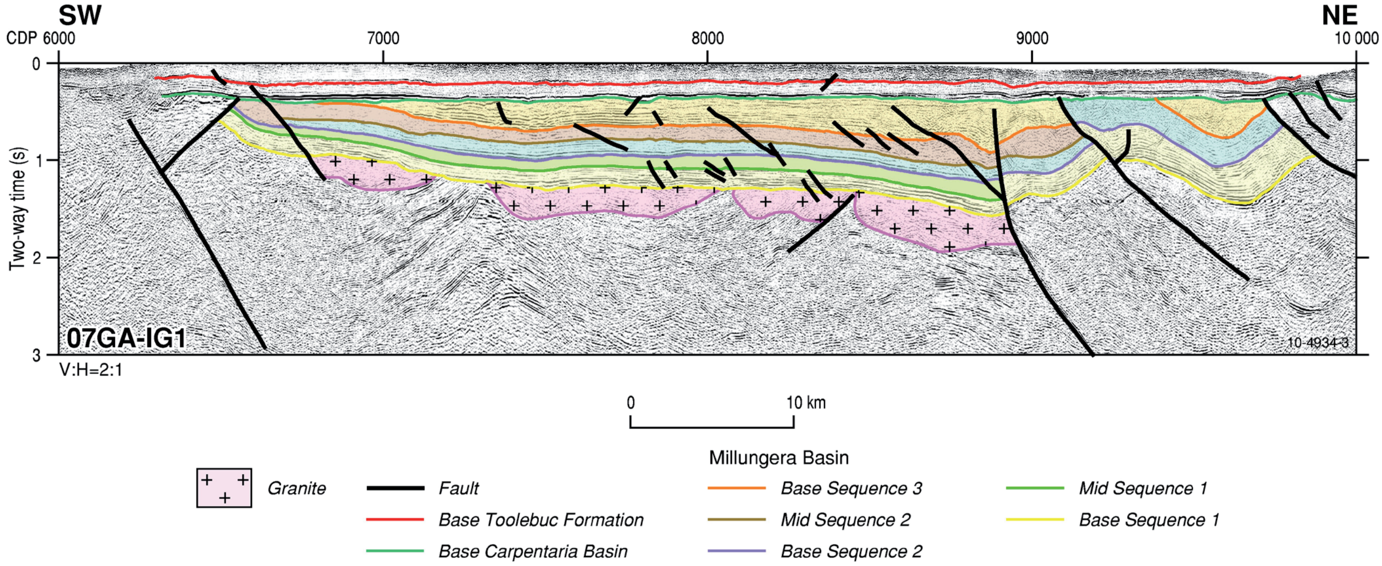

1256

1257 Figure 1b

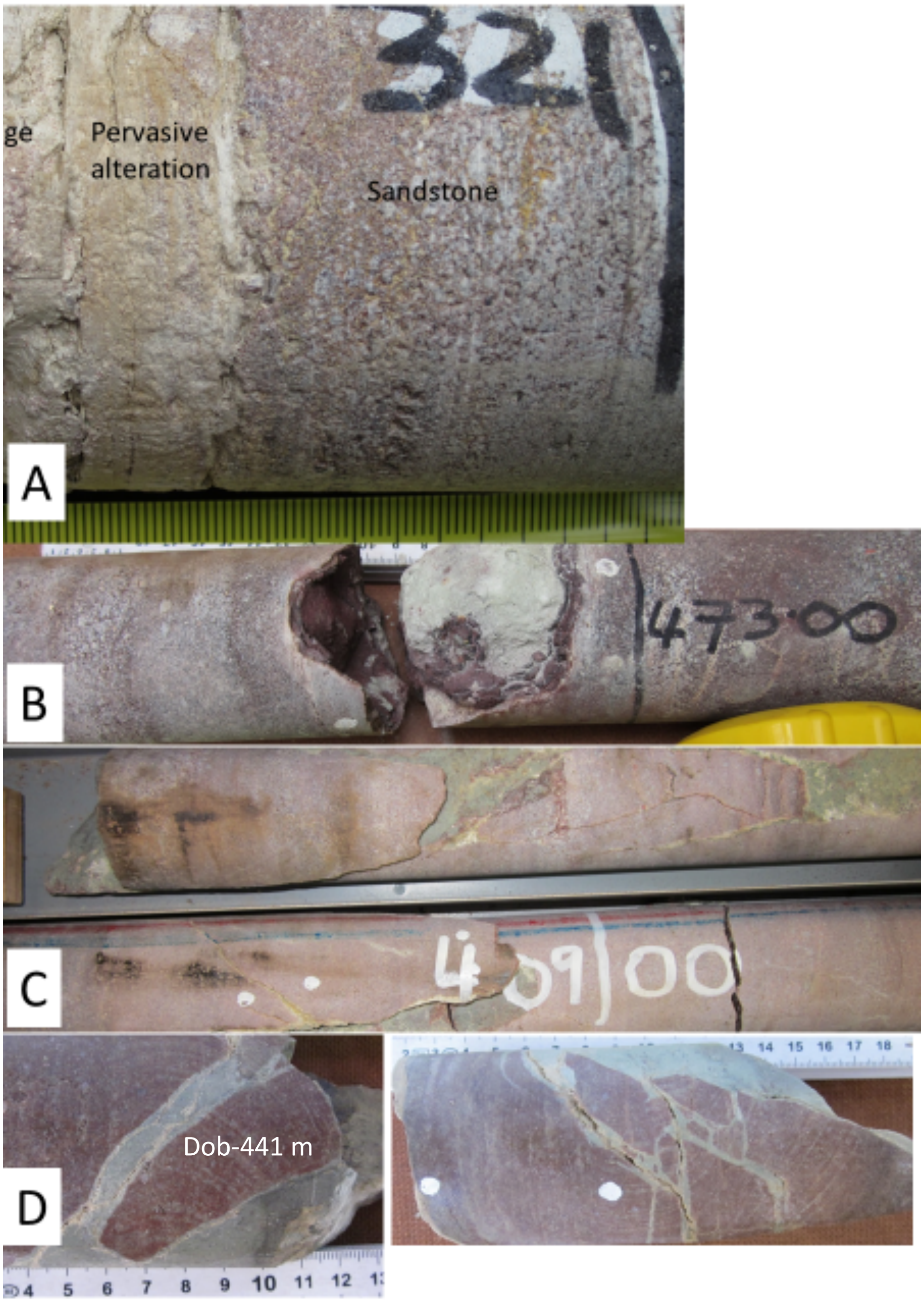
ge
Pervasive
alteration
Sandstone
321
A
473.00
B
C
D
Dob-441 m

Fig. 2

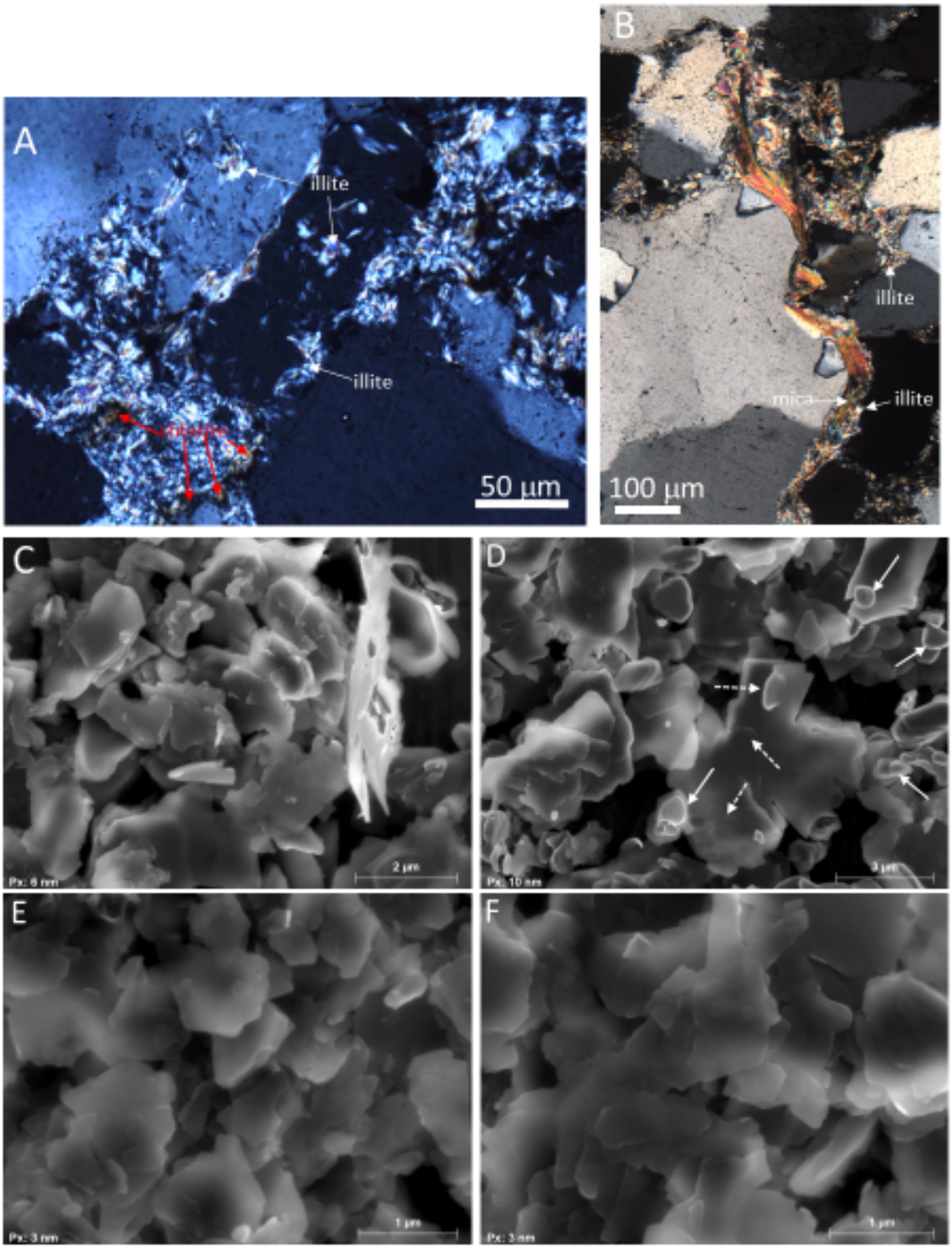
A
illite
illite
illite
chlorite
50 µm
B
illite
mica
illite
100 µm
C
D
E
F

Figure 3.

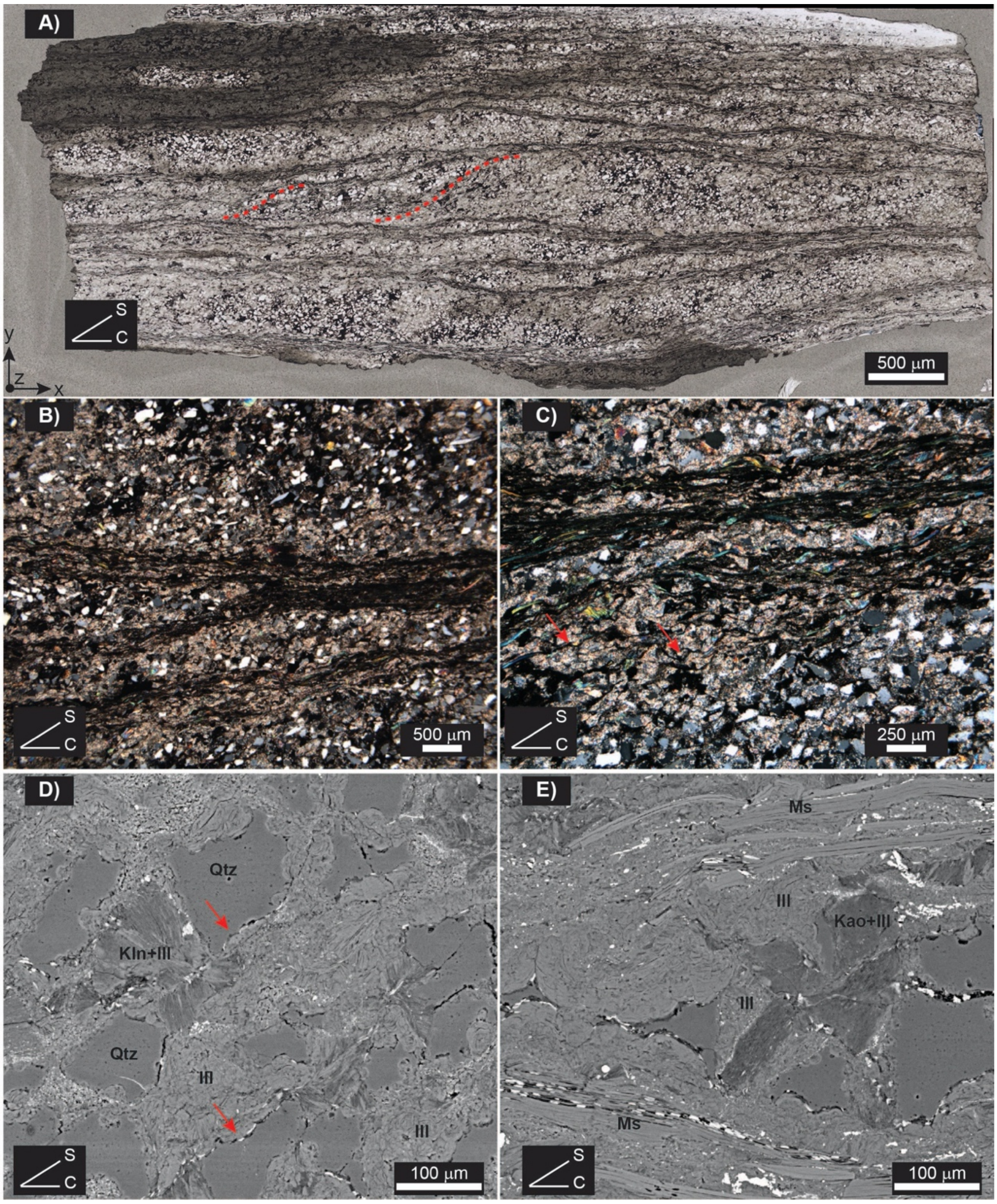
A)
S
C
y
z
x
500 μm
B)
S
C
500 μm
C)
S
C
250 μm
D)
Qtz
Kln+Ill
Qtz
Ill
Ill
S
C
100 μm
E)
Ms
Ill
Kao+Ill
Ill
Ms
S
C
100 μm

Figure 4

1263 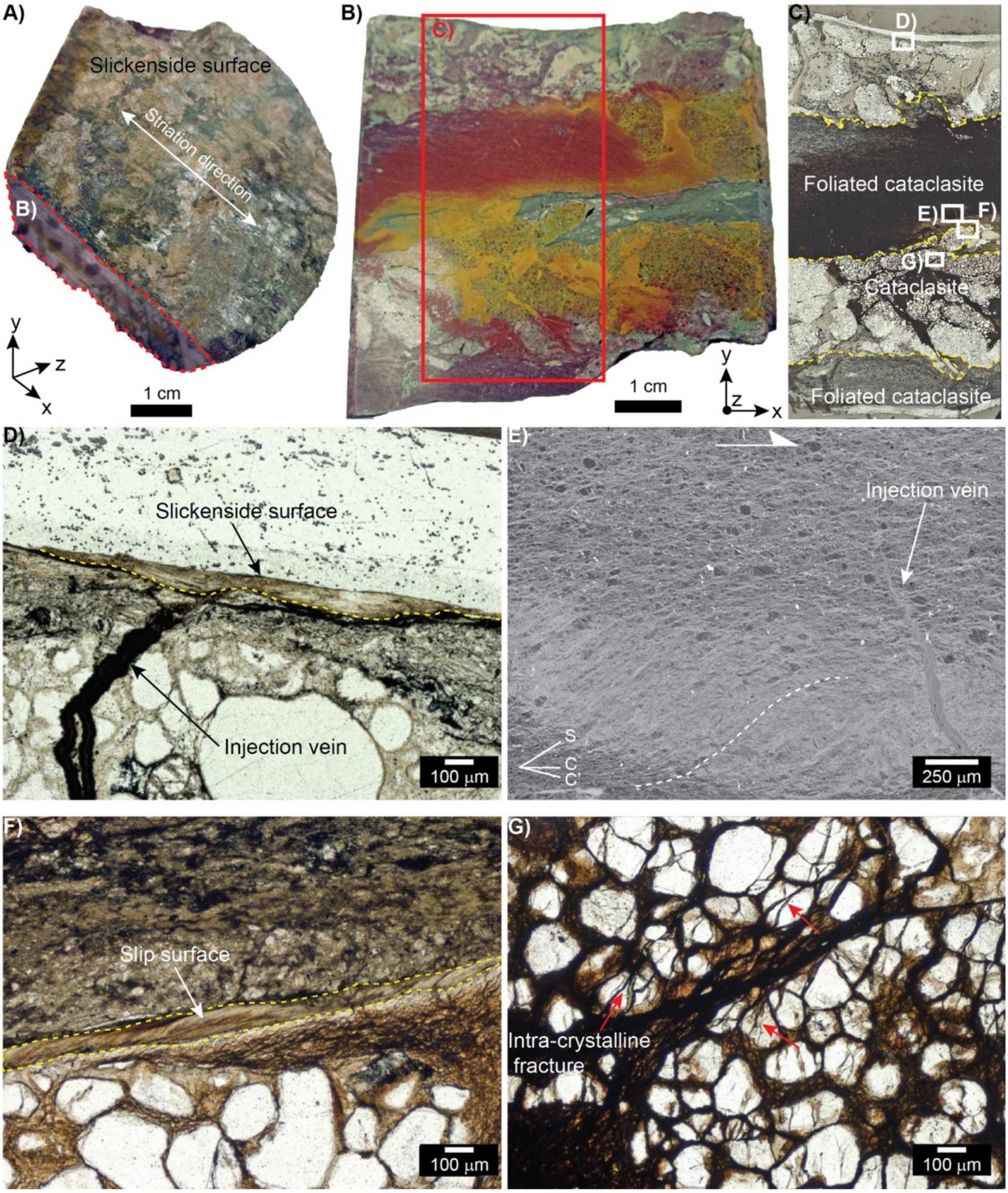

1264 Figure 5

1265

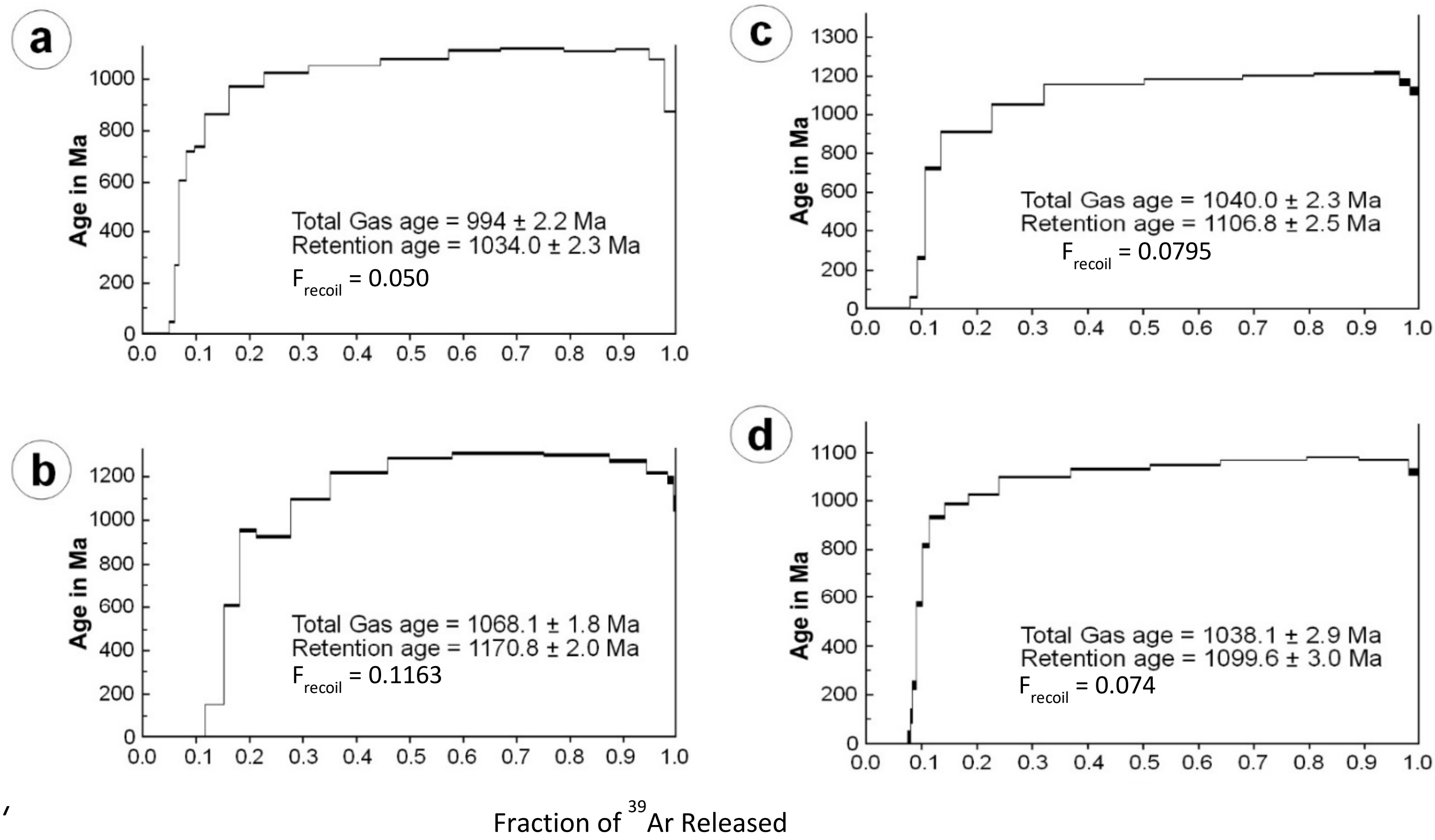
a
Age in Ma
Total Gas age = 994 ± 2.2 Ma
Retention age = 1034.0 ± 2.3 Ma
F_{recoil} = 0.050
b
Age in Ma
Total Gas age = 1068.1 ± 1.8 Ma
Retention age = 1170.8 ± 2.0 Ma
F_{recoil} = 0.1163
c
Age in Ma
Total Gas age = 1040.0 ± 2.3 Ma
Retention age = 1106.8 ± 2.5 Ma
F_{recoil} = 0.0795
d
Age in Ma
Total Gas age = 1038.1 ± 2.9 Ma
Retention age = 1099.6 ± 3.0 Ma
F_{recoil} = 0.074
Fraction of ^{39}Ar Released

Figure 6

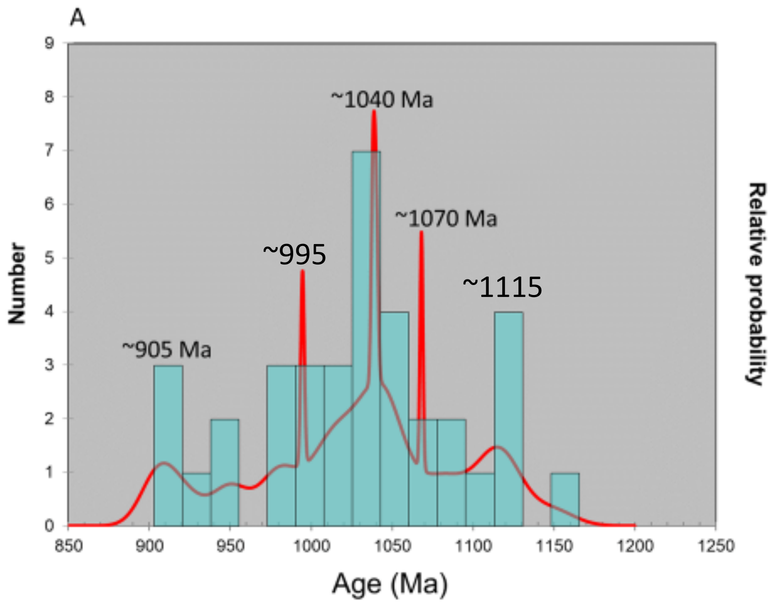

Figure 7a

B

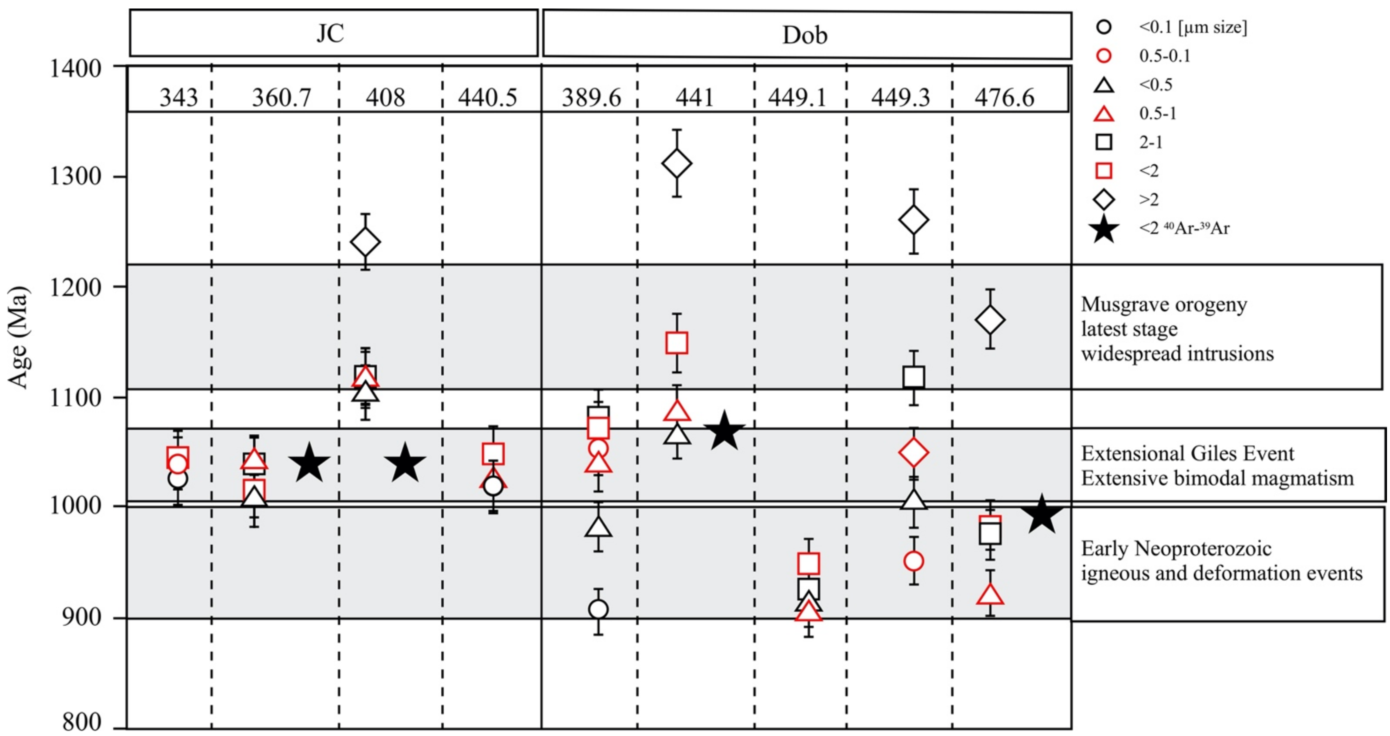

Fig. 7b

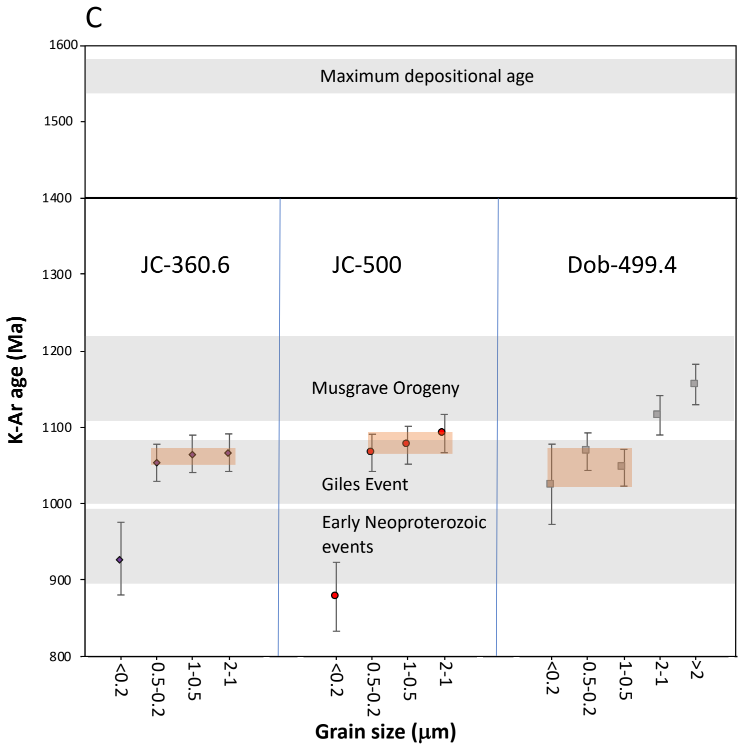

Figure 7c

1284

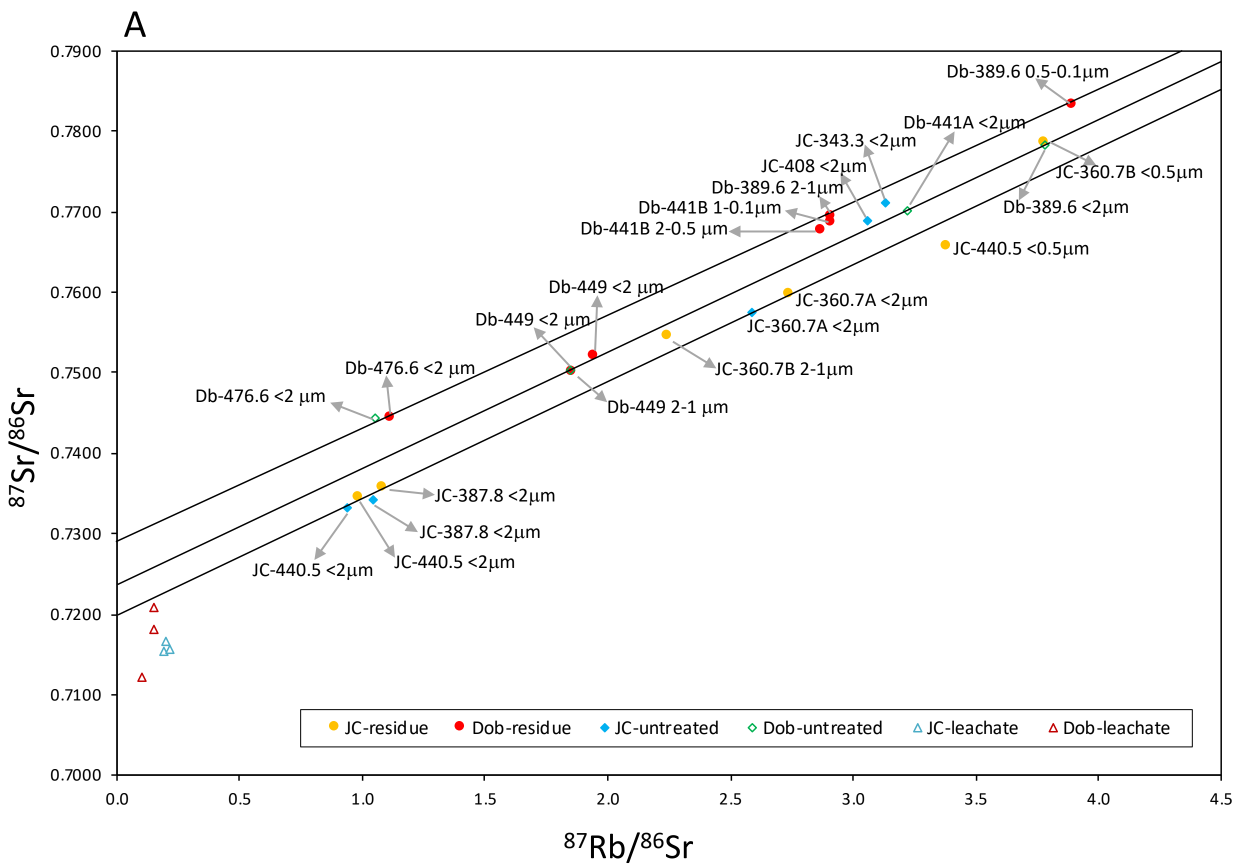

Figure 8a

1285

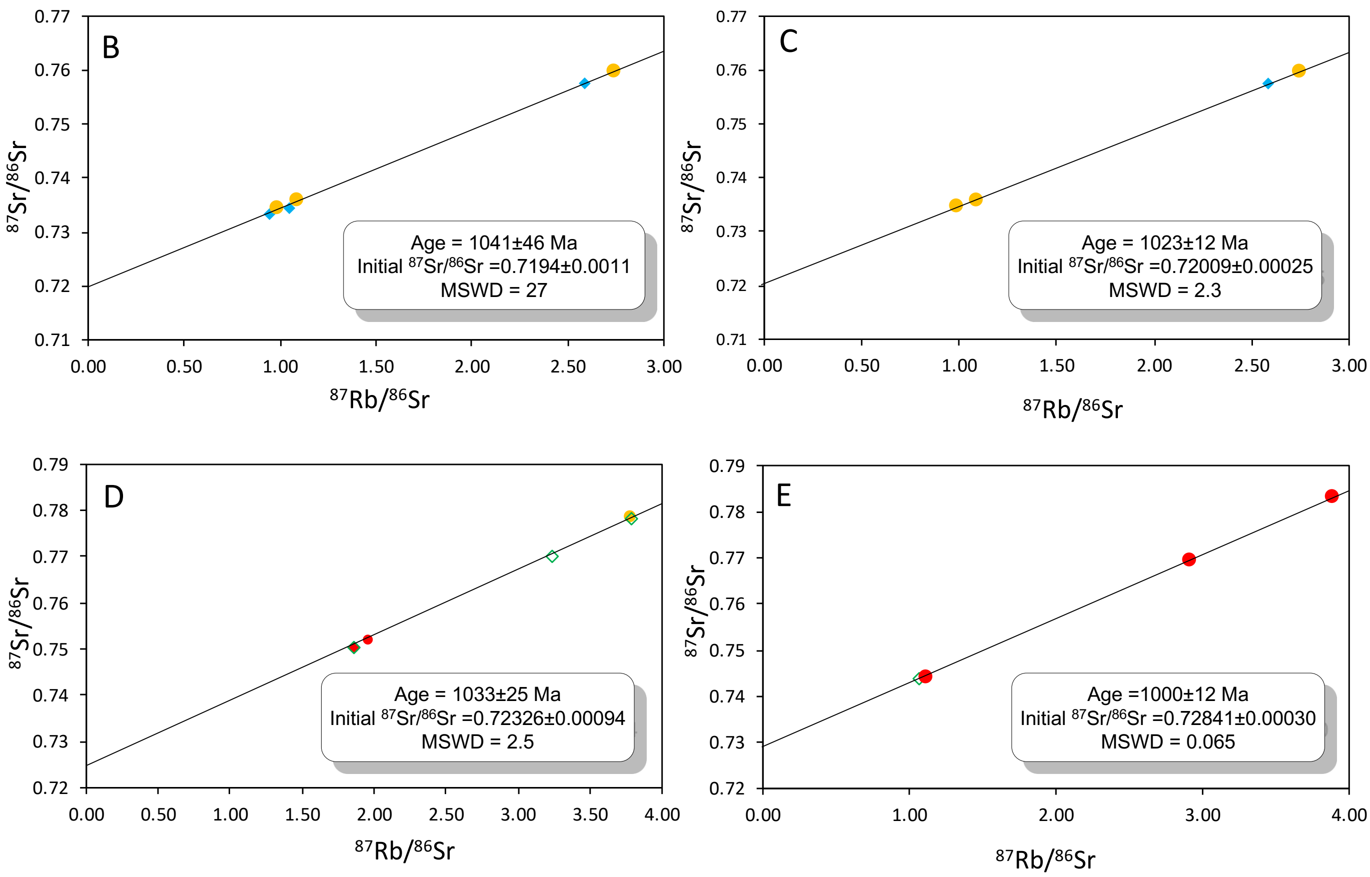
B
Age = 1041±46 Ma
Initial 87Sr/86Sr =0.7194±0.0011
MSWD = 27
C
Age = 1023±12 Ma
Initial 87Sr/86Sr =0.72009±0.00025
MSWD = 2.3
D
Age = 1033±25 Ma
Initial 87Sr/86Sr =0.72326±0.00094
MSWD = 2.5
E
Age =1000±12 Ma
Initial 87Sr/86Sr =0.72841±0.00030
MSWD = 0.065
87Sr/86Sr
87Rb/86Sr

Figure 8b-e

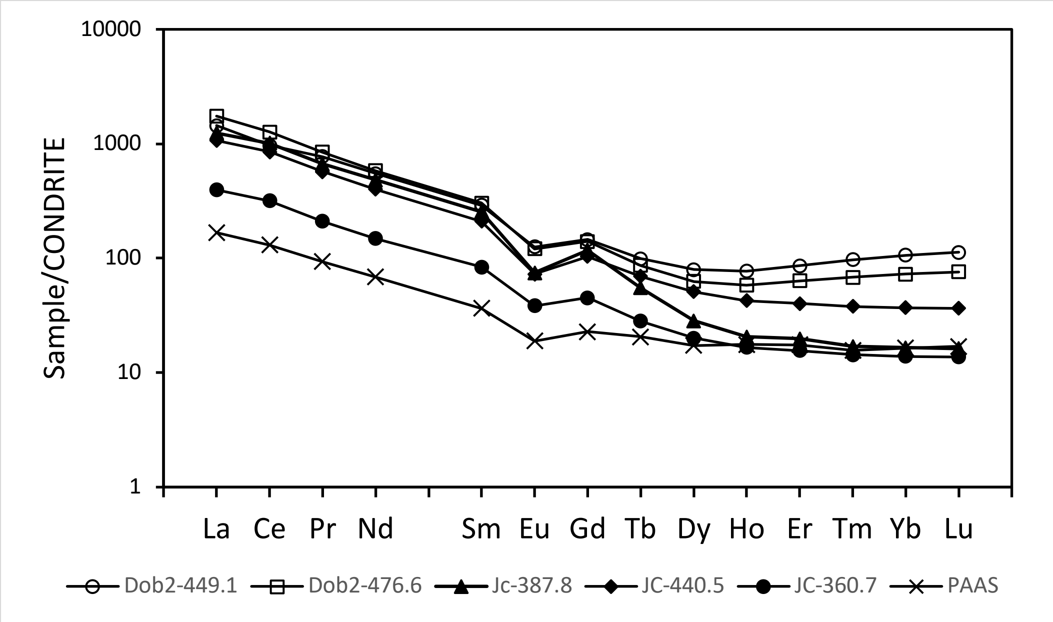
Sample/CONDRITE
10000
1000
100
10
1
La
Ce
Pr
Nd
Sm
Eu
Gd
Tb
Dy
Ho
Er
Tm
Yb
Lu
Dob2-449.1
Dob2-476.6
Jc-387.8
JC-440.5
JC-360.7
PAAS

Figure 9

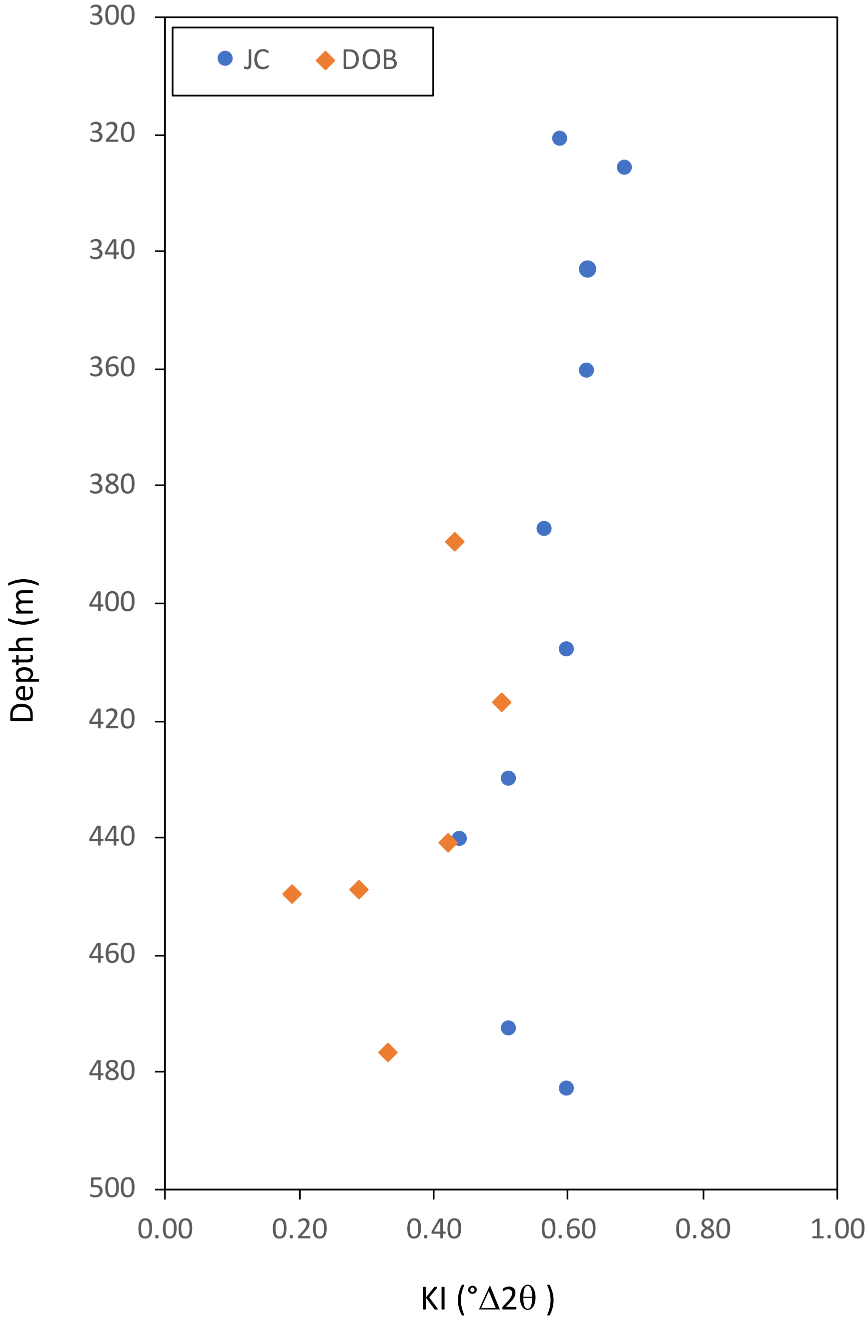
JC
DOB
Depth (m)
300
320
340
360
380
400
420
440
460
480
500
0.00
0.20
0.40
0.60
0.80
1.00
KI (°Δ2θ)

Figure 10

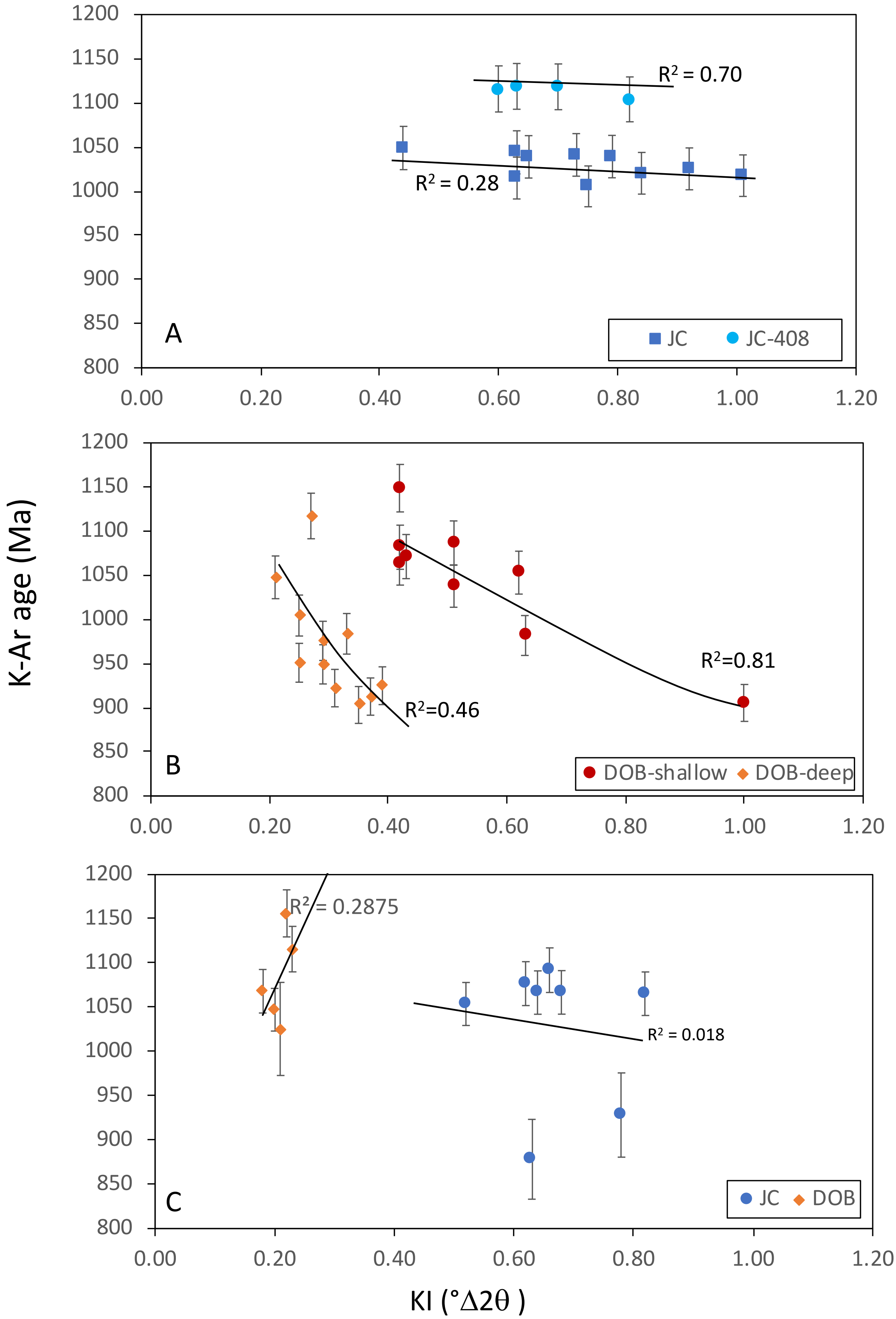
K-Ar age (Ma)
A
R^2 = 0.70
R^2 = 0.28
JC
JC-408
B
R^2=0.81
R^2=0.46
DOB-shallow
DOB-deep
C
R^2 = 0.2875
R^2 = 0.018
JC
DOB
KI (°Δ2θ)

Figure 11

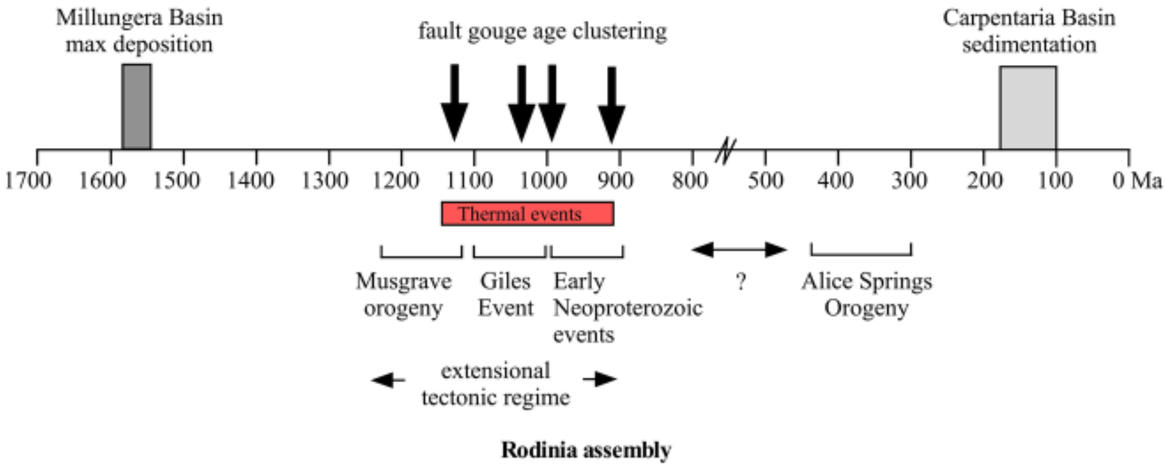
Millungera Basin
max deposition
fault gouge age clustering
Carpentaria Basin
sedimentation
1700 1600 1500 1400 1300 1200 1100 1000 900 800 500 400 300 200 100 0 Ma
Thermal events
Musgrave
orogeny
Giles
Event
Early
Neoproterozoic
events
?
Alice Springs
Orogeny
extensional
tectonic regime
Rodinia assembly

Figure 12